HHS Public Access

Author manuscript

*Cell Rep*. Author manuscript; available in PMC 2023 October 16.

Published in final edited form as:

*Cell Rep*. 2023 September 26; 42(9): 113047. doi:10.1016/j.celrep.2023.113047.

# Molecular, metabolic, and functional CD4 T cell paralysis in the lymph node impedes tumor control

**Mengdi Guo**[1,2], **Diala Abd-Rabbo**[1], **Bruna C. Bertol**[1], **Madeleine Carew**[1], **Sabelo Lukhele**[1], **Laura M. Snell**[1,3], **Wenxi Xu**[1], **Giselle M. Boukhaled**[1], **Heidi Elsaesser**[1], **Marie Jo Halaby**[1], **Naoto Hirano**[1,2], **Tracy L. McGaha**[1,2], **David G. Brooks**[1,2,4,*]

[1]Princess Margaret Cancer Centre, University Health Network, Toronto, ON, Canada

[2]Department of Immunology, University of Toronto, Toronto, ON, Canada

[3]Department of Microbiology and Immunology and Simon Comprehensive Cancer Center, Indiana University School of Medicine, Indianapolis, IN, USA

## SUMMARY

CD4 T cells are central effectors of anti-cancer immunity and immunotherapy, yet the regulation of CD4 tumor-specific T ($T_{TS}$) cells is unclear. We demonstrate that CD4 $T_{TS}$ cells are quickly primed and begin to divide following tumor initiation. However, unlike CD8 $T_{TS}$ cells or exhaustion programming, CD4 $T_{TS}$ cell proliferation is rapidly frozen in place by a functional interplay of regulatory T cells and CTLA4. Together these mechanisms paralyze CD4 $T_{TS}$ cell differentiation, redirecting metabolic circuits, and reducing their accumulation in the tumor. The paralyzed state is actively maintained throughout cancer progression and CD4 $T_{TS}$ cells rapidly resume proliferation and functional differentiation when the suppressive constraints are alleviated. Overcoming their paralysis established long-term tumor control, demonstrating the importance of rapidly crippling CD4 $T_{TS}$ cells for tumor progression and their potential restoration as therapeutic targets.

## In brief

How tumor-specific CD4 T cells differentiate and are regulated in response to tumors is not well understood. Guo et al. report that Tregs and CTLA4 rapidly program a dysfunctional CD4 T cell state in the lymph nodes that reduces tumor control.

## Graphical Abstract



*Correspondence: dbrooks@uhnresearch.ca.

[4]Lead contact

AUTHOR CONTRIBUTIONS

M.G. and D.G.B. designed the research. M.G., B.B., M.C., S.L., L.M.S., H.E., and M.J.H. performed the experiments. N.H. and T.L.M. provided the reagents. M.G., D.A.-R., W.X., G.M.B., and D.G.B. analyzed the data. L.M.S., W.X., N.H., and T.L.M. provided intellectual and technical input and discussion. M.G. and D.G.B. wrote the manuscript.

DECLARATION OF INTERESTS

The authors declare no competing interests.

SUPPLEMENTAL INFORMATION

Supplemental information can be found online at https://doi.org/10.1016/j.celrep.2023.113047.

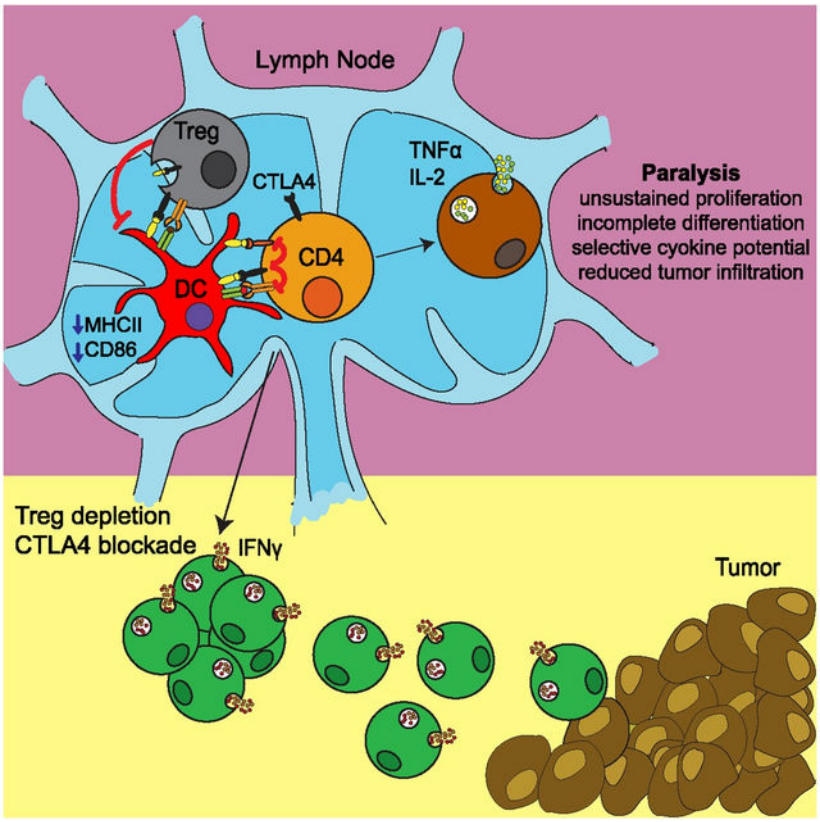


## INTRODUCTION

Attenuation and deletion of T cell function underlies the inability to control tumor growth and forms the basis for immune-restorative therapies.[1,2] Since CD8 T cells are the endpoint effectors of cancer cell killing, most studies focus on their mechanisms of dysfunction. However, increasing evidence indicates the importance of CD4 T helper (Th) cells in controlling tumor growth and increasing efficacy of immunotherapies,[3–6] suggesting the need to better understand the molecular mechanisms that regulate their differentiation in response to cancer. Importantly, CD4 $T_{TS}$ cells and CD8 T cells possess different sensitivity toward immune checkpoint blockade[7] and, as a result, likely are mediated by different regulatory mechanisms. Following activation, naive CD4 T cells differentiate into specific subsets, based on signals from the antigenic environment and interactions with antigen-presenting cells (APCs). The CD4 Th response is guided to control individual types of insults, with misdirection potentially leading to ineffective disease control. In chronic viral infections, although initially activated correctly, the increased and ongoing antigen stimulation and inflammation attenuate CD4 T cell function, skewing immune responses, disease control, and response to immunotherapy.[8–11] Mechanistically, the ongoing T cell receptor (TCR) stimulation, prolonged type I interferon (IFN-I) signaling, and upregulated suppressive molecules (e.g., IL-10, PD1:L1) elicited by chronic virus replication drive the loss of CD8 T cell helping CD4 Th1 cells and induce their trans-differentiation into B

cell helping CD4 T follicular helper (Tfh) cells,[11,12] leading to the progressive loss of virus-specific CD8 T cells.[12,13]

Prolonged antigenic stimulation and many of the inflammatory and suppressive states observed in chronic viral infections can also occur within the tumor microenvironment (TME).[2,14] Thus, alterations described in chronic infection may also impact anti-tumor immune responses. Studies using mouse models to understand anti-tumor CD4 T cell function have primarily focused on bulk CD4 T cells[7] (i.e., not antigen specific), and generally rely on *in vitro* activation prior to transfer (and usually into mice with established tumors), which, although informative, do not address how CD4 $T_{TS}$ cells are activated and develop from tumor initiation. Furthermore, for understandable reasons, clinical studies characterize total CD4 T cells in cancer patients without known antigen specificity. Thus, there is limited understanding of how naive CD4 $T_{TS}$ cells are initially activated and then differentiate in response to tumor progression. Recent TCR sequencing studies in colorectal carcinoma and breast cancer patients suggest that some tumor-infiltrating regulatory T cells (Tregs) and effector CD4 T cells share common clonal origins,[15–17] suggesting that tumor-specific Th cells can be driven to regulatory phenotypes promoting tumor progression. However, these studies are associative and, thus, it is important to define how CD4 $T_{TS}$ cells are activated, regulated, and differentiate in cancer.

Herein, we demonstrate that CD4 $T_{TS}$ cells were initially primed following tumor initiation but then rapidly frozen into a state unique to the tumor draining lymph node (dLN) environment and distinct from the T cell exhaustion induced by chronic virus infections. The tumor-induced state of CD4 $T_{TS}$ cells reduced tumor infiltration and impeded tumor control. Molecular and cellular interrogation of the CD4 $T_{TS}$ cells identified programs including abrogated Th fate commitment and transcriptional activation, a metabolic program failing to engage glycolysis and pushing toward oxidative phosphorylation (OXPHOS), increased expression of proteins involved in the tricarboxylic acid (TCA) cycle, reduced proteins involved in mitochondrial ATP production, and increased pathways of cellular stress. The CD4 $T_{TS}$ cell state was not due to chronic antigenic stimulation or PD1:PDL1 interactions, but instead was mediated by a coordination of Treg cells and CTLA4 signaling that reduced APC and T cell activation early after priming. In contrast, CD8 $T_{TS}$ cells did not exhibit the blunted proliferation or reduced tumor infiltration. Overcoming the blunted proliferative and functional state enabled robust CD4 $T_{TS}$ cell tumor infiltration and enhanced tumor control, thus defining a CD4 T cell-directed mechanism of tumor-driven immune escape.

## RESULTS

### CD4 T cells are critical for anti-tumor immune responses and their amplification can enable long-term tumor control

To understand how the CD4 T cell response is regulated in response to tumors, we identified murine tumor models wherein CD4 T cells contributed to long-term control. While the growth of B16-F10 (melanoma) was not affected by the absence of CD4 T cells, both PyMT (orthotopic breast tumor) and MC38 (colon adenocarcinoma) exhibited accelerated growth in CD4 knockout (KO) mice compared with wild-type (WT) mice (Figures 1A and S1A). This accelerated growth in CD4 KO mice was counter to what would be expected from

the loss of Tregs alone; and, indeed, early Treg depletion did enhance MC38 and PyMT tumor control (Figure S1B), indicating that the absence of conventional CD4 T cells in the CD4KO mice outweighed the beneficial effect of Treg depletion. Based on its requirement for CD4 T cells and prolonged growth time (~40–60 days to reach endpoint) allowing for the establishment of a chronic tumor: immune interaction, we primarily focused on the PyMT model. Results were then confirmed using the MC38 tumor model.

It is difficult to distinguish tumor-specific from "bystander" CD4 T cells within the TME and dLN based on phenotypic proteins. To directly analyze the CD4 $T_{TS}$ cells, we created PyMT and MC38 cell lines expressing the lymphocytic choriomeningitis virus (LCMV)-glycoprotein $(GP)_{1–100}$ sequence. These new lines (PyMG and MC38GP) express the LCMV-$GP_{61–80}$ epitope and the LCMV-$GP_{33–41}$ epitope as model tumor antigens to allow *in vivo* identification of CD4 $T_{TS}$ cells and CD8 T cells, respectively. These new lines develop into lethal tumors in regular C57BL/6 mice, indicating that insertion of the LCMV-derived sequences did not significantly enhance the immunogenicity of these tumors in the single-cell clones used herein (Figure S1C). We first determined whether enhancing CD4 $T_{TS}$ cell help would increase tumor control. For this, bone marrow-derived dendritic cells (bmDCs) were generated from β2-microglobulin−/− mice (β2m−/−, lacking MHC I expression and incapable of stimulating CD8 T cells) and pulsed with MHC II-restricted LCMV-$GP_{61–80}$ peptide or left unlabeled. In this way, only the $GP_{61–80}$-specific CD4 T cells are activated by the bmDCs. Transfer of the $GP_{61–80}$ peptide-labeled β2m−/− bmDCs alone decreased PyMG tumor growth (Figure S1D), and tumor control was further enhanced by adoptively transferring naive TCR transgenic $GP_{61–80}$-specific CD4 T cells (i.e., SMARTA cells) to increase the initial precursor frequency of CD4 $T_{TS}$ cells (Figure 1B). The transfer of $GP_{61–80}$-labeled β2m−/− bmDCs also increased and sustained tumor-specific CD4 SMARTA T cell tumor infiltration (Figure S1E). In contrast, tumor infiltration by CD4 $T_{TS}$ cells was almost entirely absent in the mice receiving unlabeled bmDCs (Figure S1E). Furthermore, transferring $GP_{61–80}$-labeled β2m−/− bmDCs 21 days after tumor initiation induced better tumor control (Figure S1F). Together these observations indicate that, while exerting a beneficial effect, the CD4 $T_{TS}$ cell response remains suboptimal.

## CD4 $T_{TS}$ cell proliferation is initiated but unsustained following activation in the draining lymph node

To understand the basis for the sub-optimal CD4 T cell help, we adoptively transferred naive CD4 SMARTA $T_{TS}$ cells prior to PyMG implantation. By day 8 after PyMG implantation (when the tumor was barely palpable, <50 $mm^3$), about 40% of the CD4 SMARTA $T_{TS}$ cells in the dLN had divided (Figures 1C and S2A). Furthermore, the proliferated cells upregulated activation-induced proteins CD44, CD86, and Ki67, indicating cell cycling (Figures 1D and S2B). Despite the division and cell activation within the dLN, very few CD4 $T_{TS}$ cells infiltrated the tumor by day 8, and the amounts did not robustly increase with tumor progression (Figure 1E), although those that did infiltrate had completely diluted the proliferation dye (Figure S2C), suggesting that extensive proliferation is requisite for tumor infiltration.

The initial activation failed to sustain cell division in the dLN. Instead, the CD4 $T_{TS}$ cells were frozen in their proliferation cycle, with a progressive loss of actively cycling Ki67+ cells and minimal subsequent cell division during tumor progression (Figures 1C and 1D). Tumor progression was accompanied by a numerical decrease in the number of CD4 $T_{TS}$ cells in the dLN, with the reduction similarly observed in each cell division peak (Figures 1C and S2D). Furthermore, the loss of CD4 $T_{TS}$ cells in the dLN was not accompanied by a comparable appearance in the tumor (Figure 1E), suggesting that the decreased number was due to an attrition of CD4 $T_{TS}$ cells as tumor growth progressed. A similarly blunted proliferation was observed for tumor-specific CD4 SMARTA T cells responding to MC38GP tumors, and for OT-II cells responding to ovalbumin-expressing MC38 tumors (Figure S2E), demonstrating that this phenotype occurs in multiple tumor models and with different TCR specificities. In contrast, CD8 $T_{TS}$ cells continued to proliferate, were numerically sustained in the dLN, and progressively infiltrated the tumor (Figures S2F and S2G), indicating that the proliferative defect was specific to CD4 T cells. Importantly, the blunted proliferation was not due to the loss of $GP_{61–80}$ expression or a progressive failure of APCs to present antigen *in vivo* since naive CD4 SMARTA T cells transferred 21 days after tumor-initiation were activated and proliferated (Figure S2H). However, these late-transferred CD4 $T_{TS}$ cells also experienced a blunted proliferation (Figure S2H), indicating the continual maintenance of mechanisms that initially allow priming, but then inhibit the clonal expansion of the CD4 $T_{TS}$ cells. Importantly, the priming at 21 days after tumor initiation shows that neither the cell transfer nor provision of dead cells at the time of tumor transplant are responsible for the blunted inhibited proliferation, but instead that this is a physiologic response of CD4 T cells to priming and growth during tumor progression.

## Limited CD4 $T_{TS}$ cell linage commitment and restricted function through tumor progression

In addition to their blunted proliferation, CD4 $T_{TS}$ cells in the dLN at the early stage of tumor (day 8) failed to express most Th-defining transcription factors, including Tbet (Th1), RORgT (Th17), or FoxP3 (Treg) (Figures 2A and S3A). Conversely, the majority of the CD4 $T_{TS}$ cells expressed and maintained high levels Bcl6 and TCF1 (Figure 2A). Virus-specific CD4 T cells from chronic LCMV-clone 13 (Cl13) infection are shown for comparison to identify Th1 (Tbet+) and Tfh (Bcl6+) and the expression of these lineage defining proteins (Figure 2A). In comparison, Bcl6 was not expressed in the naive CD4 T cells, while TCF1 was continuously expressed at high levels in CD4 $T_{TS}$ cells (Figures 2A and S3B), indicating that the CD4 $T_{TS}$ cells are being activated, but not sufficiently to downregulate TCF1 expression from naive cell levels. This diminished activation level is further supported by the low expression of the TCR-induced co-stimulatory molecule CD27[18] (Figure 2A). Increased Bcl6 and TCF1 are associated with Tfh differentiation; however, the CD4 $T_{TS}$ cells had much lower expression of other Tfh-lineage-defining and functional proteins, including CXCR5 or ICOS, compared with the virus-specific Th1 and Tfh that are generated during chronic LCMV infection (Figure 2B), suggesting that these cells are not Tfh committed. Furthermore, the CD4 $T_{TS}$ cells produced high levels of IL-2 and TNF-α in response to antigen, but minimal IFN-γ or IL-10 (Figures 2C, S3C, and S3D), indicating restricted, yet specific, cytokine producing potential through cancer progression. By 30 days after PyMG initiation, 10%–40% of the CD4 $T_{TS}$ cells in the dLN had upregulated FoxP3,

with most of the FoxP3-expressing cells having proliferated extensively (Figure 2D). Within the tumor, despite low amounts of CD4 $T_{TS}$ cells, the majority expressed FoxP3 at day 30 but not day 8 (Figure 2D), suggesting that tumor-specific CD4 Treg cells preferentially and progressively accumulate in the tumor.

We next performed mass cytometry (CyTOF) analyses of CD4 $T_{TS}$ cells in the dLN throughout PyMG progression. Phenograph-based clustering of the CyTOF data resolved nine clusters that could be broadly grouped into three major categories: (1) naive-like cells expressing high CD62L, in combination with low activation-induced proteins (cluster [c] 9), (2) activated populations (c1–c7), and (3) induced Treg (iTreg) cells (c8) (Figure 2E). Despite the ongoing antigen presentation, the frequency of naive (c9) and all the effector populations of CD4 $T_{TS}$ cells (c1–c7) remained relatively stable with limited changes in their expression of activation, inhibitory, or Th-lineage-defining transcription factors during tumor progression (Figures 2E, S3E, and S3F). The exception was the appearance between days 15 and 30 of a tumor-specific FoxP3+ Helios+ iTreg population (c8) that expressed proteins associated with Treg function (e.g., CD25, CD73, CD39, CTLA4, and CD39), and in general had the highest activation level among all tumor-specific CD4 T cell clusters (Figures 2E and S3E). Interestingly, the iTregs also expressed Th1-lineage-defining proteins, including Tbet and SLAMF1 (Figures 2E and S3G), suggesting that tumor-specific iTregs develop Th1-like features that could further limit antigen-specific CD4 and CD8 T cells.[9]

To gauge the expression level of activation-induced proteins on CD4 SMARTA $T_{TS}$ cells, we compared them with the same CD4 SMARTA T cells activated during chronic LCMV-Cl13 infection. Unlike the virus-specific SMARTA T cells that expressed high levels of activation-induced and inhibitory proteins, the CD4 $T_{TS}$ cells expressed much lower levels of these with many not expressing them at all, including CD39 or PD1 (Figure 2F). Yet, a large proportion of the CD4 $T_{TS}$ cells expressed CTLA4 (albeit less than in the chronic virus infection) (Figure 2F) suggesting preferential expression of T cell inhibitory receptors. Interestingly, the few SMARTA cells that did infiltrate tumor effectively upregulated PD1 and acquired an exhausted phenotype like that observed in various mouse tumor models and human cancers (Figure S3I).[20–22] Deeper analysis of dLN CD4 SMARTA T cells indicated that the activated populations could be further categorized based on the expression of four dominating protein expression profiles: (1) CD69-hi, CD62L-int, recently activated cells (c3), (2) Ki67+ cycling cells (c4 and c5), (3) CD73-hi populations (c2 and c7), and (4) non-cycling CD86-hi populations (mostly c1 and c6, but also with some overlap with the CD73- and the Ki67-expressing populations) (Figure 2G). Consistent with progressive loss of Ki67-expressing cells, c4 decreased in abundance rapidly (between days 8 and 15) while c5, which had upregulated Bcl6 and other activation-induced proteins, persisted longer (decreasing between days 15 and 30) (Figure S3E). While the CD86-hi c1 and c6 remained stable within the CD4 $T_{TS}$ cell population, the frequency of CD73-hi clusters increased during the late stage of tumor progression (Figures 2G and S3E). Counter-intuitively, Bcl6 and Blimp1 (transcription factors that generally repress each other[23]) were co-expressed by the Ki67+ cells (Figure S3H), further highlighting the uncommitted differentiation of the activated CD4 $T_{TS}$ cells.

The altered activation state of CD4 $T_{TS}$ cells in the dLN encompasses a multifaceted phenotype characterized by defects in sustained proliferation, Th differentiation, and acquisition of effector function. This state is distinct from T cell exhaustion. Importantly, the state is actively maintained and the CD4 $T_{TS}$ cells retain the ability to resume proliferation when adequately stimulated with antigen-pulsed DCs. Thus, since the CD4 $T_{TS}$ cells are essentially frozen after their initial priming but can resume proliferation when triggered, we use the term “paralysis” to represent this dysfunctional state in response to cancer growth.

## CD4 $T_{TS}$ cells exhibit a metabolic profile of sub-optimal activation

Metabolic reprogramming from OXPHOS to aerobic glycolysis after activation (the Warburg effect) is critical for T cell proliferation, differentiation, and function.[24,25] To probe single-cell changes in CD4 $T_{TS}$ cell metabolism, we adapted a metabolism CyTOF panel from human to mouse cells.[26] We compared naive CD4 SMARTA T cells and CD4 SMARTA T cells on day 8 after PyMG initiation, as well as CD4 Th1 and Tfh SMARTA cells from day 8 after acute LCMV-Armstrong (Arm) infection. We used the virus-specific CD4 T cell response to acute LCMV-Arm infection because it is a gold-standard to define bona fide CD4 Th1 and Tfh differentiation.[27] In this way, the same CD4 SMARTA T cells were analyzed in various conditions, thus allowing direct comparison of T cell metabolic profile. Compared with LCMV-specific Th1 and Tfh cells, the upregulation of key proteins involved in glucose uptake, GLUT1, and the glycolysis pathway, hexokinase 2 (HK2), and GAPDH, had decreased expression in CD4 $T_{TS}$ cells (Figures 3A–3C and S4A), suggesting an inhibited switching to aerobic glycolysis for energy production. Interestingly, GAPDH, a key enzyme involved in glycolysis and an important transcription regulator of T cell function,[28] was reduced even compared with naive T cells (Figures 3A, 3B, and S4A). PFKFB4, the bifunctional kinase/phosphatase that indirectly affects glycolysis by regulating the concentration of glycolytic byproduct fructose-2,6-biphosphate, was upregulated in tumor-activated CD4 T cells (Figures 3A–3C and S4A). The upregulation of PFKFB4 has been reported to be induced by hypoxia via HIFa to promote further uptake of glucose in many cancer cells and promote their survival.[29,30] Although the function of PFKFB4 in T cell is still not clear, its upregulation in CD4 $T_{TS}$ cells compared with virus-specific CD4 Th1 and Tfh cells could serve as a compensatory response to the impaired glycolysis pathway. Thus, CD4 $T_{TS}$ cells fail to increase expression of proteins to allow for effective transition to aerobic glycolysis, which could hinder their proliferation and survival.

In contrast to glycolysis, many proteins involved in OXPHOS are increased in CD4 $T_{TS}$ cells compared with virus-specific CD4 Th1 and Tfh cells. For example, key enzymes involved in the TCA cycle, such as citrate synthase and isocitrate dehydrogenase 1, and mitochondrial membrane ATP synthase complex V (ATP5A), are upregulated in CD4 $T_{TS}$ cells (Figures 3A–3C and S4A), suggesting an enhanced reliance on OXPHOS for energy production. Interestingly, the expression of cytochrome *c*, a critical protein in the electron transport chain for the generation of ATP, and other mitochondria proteins (such as DRP1, OPA1, and VDAC1) that are critical for proper mitochondria function were reduced in CD4 $T_{TS}$ cells (Figures 3A–3C and S4A), suggesting abnormal mitochondria function. Thus, CD4 $T_{TS}$ cells show decreased mitochondria function compared with virus-specific Th1

and Tfh cells, which could ultimately offset the enhanced TCA cycle and further result in deficiency in energy production.

Consistent with increased expression of proteins involved in the TCA cycle, CD4 $T_{TS}$ cells have elevated amounts of enzymes involved in glutamine metabolism, whose products directly fuel OXPHOS. Several key enzymes involved in glutamine metabolism, such as glutaminase (GLS), GOT2, and glutamate dehydrogenase 1 and 2 were significantly elevated in CD4 $T_{TS}$ cells (Figures 3A–3C and S4A). Interestingly, elevated levels of GLS and glutamine metabolism have been reported to inhibit Th1 differentiation,[31] suggesting a possible role of enhanced glutamine metabolism in the inhibition of Th1 differentiation of CD4 $T_{TS}$ cells. The enzymes involved in lipid metabolism exhibited more complex regulation patterns. For example, medium-chain acyl-CoA dehydrogenase had increased levels in CD4 $T_{TS}$ cells, whereas CPT1A was decreased (Figures 3A–3C and S4A). Intriguingly, PPAR$\gamma$, an important protein regulating the uptake of fatty acids and cholesterol balance in adipocytes and macrophages[32–35] was minimally upregulated in CD4 $T_{TS}$ cells compared with naive cells and was diminished compared with virus-specific CD4 Th1 and Tfh cells (Figures 3A–3C and S4A). NRF1, an endoplasmic reticulum protein that directly senses cholesterol accumulation,[36] was elevated in CD4 $T_{TS}$ cells (Figures 3A–3C and S4A). Altogether, the abnormal expression of PPAR$\gamma$ and NRF1 suggest a dysregulation of lipid metabolism, especially cholesterol, in CD4 $T_{TS}$ cells.

To evaluate the overall changes of each metabolic pathway, we calculated the scores of each metabolic pathway on the single-cell level by summarizing the expression of key enzymes directly involved in each pathway, as described in Hartmann et al.[26] Indeed, CD4 $T_{TS}$ cells showed lower scoring in glycolysis, and significantly higher scoring in glutamine and OXPHOS (Figure 3D). Thus, CD4 $T_{TS}$ cells exhibit signs of failure to transition to aerobic glycolysis, and instead appear to have a preference to use glutamine for energy and skewing toward OXPHOS despite an abnormal mitochondria metabolic state that could ultimately impair the ATP production.

## Transcriptional programming and differentiation of CD4 $T_{TS}$ cells

To understand the programming guiding CD4 $T_{TS}$ cell differentiation, we performed single-cell RNA sequencing (scRNA-seq) on SMARTA CD4 $T_{TS}$ cells from the dLN on day 8 after PyMG initiation. Clustering the CD4 $T_{TS}$ cells revealed seven clusters (Figure 4A). c6 (enriched with activation-associated genes *Egr1,2,3, Rel, Nr4a1, Nfatc1, Cd40l*, and *Id3*) and c7 (enriched with interferon-stimulated genes *Ifit1, Ifit3, Isg15, Isg20, Bst2, Stat1*, etc.) each constituted less than 5% of the sample and were not further characterized in the following analysis (Figure 4B). c3 expressed the highest levels of *Sell* (encoding CD62L) and *Il7r*, indicating these as the naive-like population of CD4 $T_{TS}$ cells (Figure 4B). However, c3 also exhibited increased expression of *Jun* and *Fos* (together forming the AP-1 signaling complex),[37] and *Cd69*, a gene stimulated early following TCR engagement (Figure 4B), indicating that these cells have encountered antigen, but were frozen in a naive-like state. c4 and c5 were enriched in genes involved in cell cycling. c4 was specifically enriched in protein translation (*Eif5a, Ddx21*, etc.), ribosome biosynthesis (*Ncl, Nop58, Pa2g4, Fbl*, etc.), and mitochondria function (*C1qbp, Hspd1, Atp5g1,* etc.), while c5 was

enriched for genes involved in proliferation (*Mki67, Birc5, Ccnb2, Cenpe*, etc.) and DNA replication (*Pclaf, Top2a*, etc.) (Figure 4B), indicating that c4 and c5 are in different phases of cell cycle. The largest activated populations, c1 and c2 (comprising over 50% of the CD4 SMARTA $T_{TS}$ cells) were enriched in genes that diminish T cell activation, including *Izumo1r* (FR4, associated with T cell anergy),[38] *Rgs10* (restricts T cell adhesion and integrin expression),[39] and *Pdcd4* (restricts T cell *in vitro* expansion)[40] (Figure 4B). Interestingly, recent studies have suggested that *Pdcd4* transcription is induced by CTLA4 (the most upregulated inhibitory receptor on the CD4 $T_{TS}$ cells; Figure 2F) via FOXO1 nuclear translocation,[41] suggesting an involvement of CTLA4 in the paralysis of these CD4 T cells. c2 was also enriched in negative regulatory genes, such as *Lgals1* (galectin-1),[42,43] *Pycard/Asc*,[44] and *Klf2* (associated with naive T cells and quiescent state)[45,46] (Figure 4B), suggesting that these cells have passed through the activation state of c1 and were suppressed into a resting state.

We performed Monocle[47] analysis to determine the activation and differentiation trajectory of the CD4 $T_{TS}$ cells. Starting from the naive c3, the differentiation trajectory goes through a common population (c1) then forks into three distinct paths (Figure 4C). Consistent with c1 as the first path through which the other populations progress, cells in c1 had the lowest differentiation score, a score that ranks pseudotime distance from the starting population[47–49] (Figure S4B). The first fork from c1 leads to a pathway enriched in interferon-stimulated cells (c7). At the second fork, one direction path leads to c2, with these cells having an intermediate pseudotime score (Figure S4B), consistent with their increased expression of negative regulatory genes compared with c1 (Figure 4B). The third path leads to actively dividing populations (c4 and c5) with the highest pseudotime scores (Figure S4B), suggesting that a higher differentiation state is associated with active cell cycle. Thus, most CD4 $T_{TS}$ cells are stuck in an early priming stage by day 8, upregulating genes that antagonize activation; and, although a small population are proliferating, the majority express activation-suppressing genes.

We next preformed gene set variation analysis to investigate the transcriptional pathways associated with each population. Consistent with their proliferation status, c4 and c5 highly upregulated multiple gene expression pathways involved in cell cycling, such as E2F targets, G2/M checkpoints, and DNA repair, whereas naive-like population (c3) and the paralyzed populations (c1 and c2) did not (Figure 4D, and all differentially expressed pathways in each cluster are quantified in Figure S4C). As expected, the actively proliferating cells (c4 and c5) had undergone extensive metabolic reprogramming, particularly upregulating glycolysis in parallel to high activation of the Myc pathway (required for effector T cell metabolic reprogramming). Consistent with its low differentiation status, c1 is metabolically lower for gene pathways supportive of glycolysis, OXPHOS, and fatty acid metabolism, and this population fails to activate Myc pathway (Figures 4D and S4C). Although c2 upregulated fatty acid metabolism and OXPHOS (albeit lower than the actively proliferating populations c4 and c5), c2 did not significantly upregulate glycolysis or activate Myc (Figure S4C). Interestingly, compared with proliferating cells (c4 and c5), both c1 and c2 exhibited low expression of the mTORC1 signaling pathway, a major cell-activation pathway induced by TCR signaling[50] (Figures 4D and S4C), suggesting that the proliferative paralysis and diminished metabolic reprogramming could be a result of insufficient priming. In contrast

to the metabolic and proliferation pathways, apoptosis and P53 pathways (involved in cell-cycle arrest) are activated in c1 and further enhanced in c2, but not in naive-like population (c3) or proliferating cells (c4 and c5) (Figures 4D and S4C). Altogether, these observations suggest that priming by tumor antigen fails to induce necessary cellular changes essential for sustained clonal expansion of effector CD4 T cells.

To define the global changes of T cell paralysis, we re-clustered with naive CD4 T cells. This approach yielded a dominant cluster (c4) in the cells from the tumor-bearing mice and multiple clusters in the naive cells. The dominant clusters in the CD4 $T_{TS}$ cells and naive cells were generally exclusive of each other (Figure S4D). For the analysis, the naive cells were combined, only excluding a small activated cluster 7 (Figure S4D). Compared with naive CD4 T cells, CD4 $T_{TS}$ cells exhibited a mixed Th transcriptional programming, featuring enhanced Tfh and to a lesser extent iTreg signatures, with limited Th1, Th2, and Th17 signatures (Figure 4E), consistent with the protein expression analysis by CyTOF (Figures 2A and 2B). Ingenuity Pathway Analysis (IPA) further revealed that OXPHOS and pentose phosphate pathways were activated in CD4 $T_{TS}$ cells but not glycolysis (Figure 4F). Consistent with the low protein expression (Figures 3A–3C and S4A), upstream regulator analysis indicated inhibited activity of HK2 (glycolysis) and PPAR pathways (Figures 4F and S4E), further corroborating a defect in glycolysis and PPARγ-regulated fatty acid metabolism and intracellular cholesterol balance. In addition, CD4 $T_{TS}$ cells are enriched in pathways associated with cellular stress, including NRF2-mediated oxidative stress, hypoxia, and HIF1α signaling (Figure 4F). In parallel to the oxidative stress response, pathways negatively related to survival and proliferation, such as necroptosis, senescence, and inflammasome signaling, are also activated in these CD4 $T_{TS}$ cells (Figure 4F), whereas the activity of transcription factor ID2 (important for effector T cell survival and resistance to apoptosis) is inhibited (Figure S4E). Thus, CD4 $T_{TS}$ cells fail to undergo necessary metabolic reprogramming, and exhibit abnormal cellular stress signaling and pathways negatively associated with survival.

We next measured the gene expression profiles of CD4 $T_{TS}$ cells to previously defined effector and exhaustion gene expression signatures[51–53] to understand their differentiation relationships. As a first step, all populations were individually compared with naive T cells to generate upregulated genes specific to each cell state. Comparing those upregulated genes against gene expression profiles of effector and exhausted CD4 T cells demonstrated that most upregulated genes in the CD4 $T_{TS}$ cells are unique to that subset, with 75% of the top 500 upregulated genes in the CD4 $T_{TS}$ cells being unique compared with effector or exhausted CD4 T cells (Figure 4G). Furthermore, the paralyzed CD4 cells have minimal overlap of with CD4 effector (only 12% of DEGs overlap) or exhausted (9% of DEGs overlap) T cells. The same lack of overlap is observed in relation to CD8 effector (11% overlap of upregulated genes) or exhausted (11% overlap of upregulated genes) T cells (Figure 4G). Thus, combined with the CyTOF and transcriptional data, the CD4 T cell paralysis is a distinct cellular state.

To investigate whether a similar population of CD4 T cells was present in humans, we interrogated published scRNA-seq data from the tumor dLN of patients with breast cancer[54] and lung adenocarcinoma.[55] For this analysis, we used the 373 DEGs identified in Figure

4G as the CD4 $T_{TS}$ signature. An analogous result was observed using a small core of 25 DEGs. Up to 8.3% of sequenced human dLN CD4 T cells possessed a similar gene expression to mouse paralyzed CD4 $T_{TS}$ cells (Figure S4F; Table S1); although consistent with the data in our mouse models, the frequency of these cells in the dLN was generally low. Interestingly, the number of this population was increased with lymph node metastasis. We then compared the human CD4 T cells identified against the other CD4 T cells in the sample to assemble a specific signature associated with human paralyzed CD4 T cells (Figure S4G). Biological processes GO enrichment analysis of these signature genes demonstrated that the human CD4 T cells were enriched in similar pathways as paralyzed mouse CD4 $T_{TS}$ cells, particularly those related to OXPHOS (Figure S4H). Thus, a small population of CD4 T cells in the dLN of human breast and lung cancer patients also exhibit a similar CD4 $T_{TS}$ cell transcriptional paralysis signature.

## CTLA4 blockade alleviates the proliferative paralysis but only minimally promotes differentiation

We next investigated the molecular mechanisms underlying the CD4 $T_{TS}$ cell proliferation and differentiation paralysis. Both CTLA4 and to a much lesser extent PD1 were upregulated by CD4 $T_{TS}$ cells early after activation (Figure 2F), suggesting a role for these inhibitory receptors. Consistent with its minimal expression, blocking PD1:PDL1 interactions during initial activation failed to overcome the proliferative paralysis (Figure S5A). In contrast, CTLA4 blockade completely restored the proliferation of CD4 $T_{TS}$ cells (Figure 5A). Furthermore, blocking CTLA4 in mice with established tumors (day 21) also restored CD4 $T_{TS}$ cell proliferation (Figure 5B), indicating that CTLA4 constantly maintains proliferative paralysis through tumor progression. To further investigate how CTLA4 blockade alone impacts CD4 $T_{TS}$ cell response, we used CyTOF to characterize SMARTA cells in day 8 dLN of CTLA4 blockade or isotype mice. Despite promoting proliferation, CTLA4 blockade only induced the emergence of a single cluster (c8), with minimal effect on protein expression, except for increased ICOS (Figures S5B–S5D), suggesting an uncoupling of proliferation from differentiation in CD4 $T_{TS}$ cells. The newly emergent c8 following CTLA4 blockade did express increased activation-induced proteins and appeared to be a mixed Th1-Tfh precursor (based on Tbet and Bcl6 co-expression) (Figure S5C). Both Tregs and tumor-specific CD4 T cells express CTLA4 in the dLN. Inducible deletion of CTLA4 expression on Tregs (FoxP3-icre × CTLA4fl/fl mice) before tumor implantation did not overcome the proliferative paralysis (Figure S5E), nor did CRISPR-mediated deletion of CTLA4 in SMARTA cells before transfer (Figure S5F), indicating a cooperative mechanism of CTLA4 on both Treg and CD4 $T_{TS}$ cells to inhibit proliferation.

## Tregs mediate the CD4 T cell proliferative paralysis, but their depletion reciprocally induces tumor-specific iTreg differentiation

Based on the expression of CTLA4 by Tregs, we next sought to understand how Tregs were modulating the CD4 T cell paralysis. Coinciding with the CD4 $T_{TS}$ cell paralysis was an increase in the frequency of FoxP3+ Tregs in the dLN (Figure S6A). Indeed, depleting Tregs at the time of tumor initiation using mice expressing diphtheria toxin receptor (DTR) under the control of the FoxP3 promoter (FoxP3-DTR; DREG) led to rapid CD4 $T_{TS}$ cell

proliferation in the dLN (Figures 5C and S6B) and sustained tumor infiltration (Figure 5D). A similar increased proliferation occurred when Tregs were depleted using anti-CD25 antibody (Figure S6C). Furthermore, Treg cell depletion in mice with established tumors (21 days after PyMG initiation) overcame the proliferative paralysis and induced robust CD4 $T_{TS}$ cell division (Figures 5E and S6D). Thus, Treg cells actively and continuously inhibit CD4 $T_{TS}$ cell proliferation throughout tumor progression.

In addition to overcoming the proliferative block, Treg depletion increased the activation state of CD4 $T_{TS}$ cells and drove the emergence of multiple new CD4 $T_{TS}$ cell clusters (c4–c8) (Figure 5F). Of the newly emerging cell populations after Treg depletion, c6 exhibited protein-expression patterns of Tfh-like cells with high expression of Bcl6, TCF1, and PD1, while retaining high CD62L (Figures 5F and 5G). Conversely, c4 differentiated into Th1-like cells (a subset previously unseen when Tregs were present), expressing Tbet, Blimp1, Tim3, and Lag3, combined with low expression of TCF1 and Bcl6 (Figures 5F and 5G). Further, both the Th1-like c4 and the Tfh-like c6 had higher expression of CD27, CD127, and Ki67 (Figure S6E), suggesting increased activation and survival. Strikingly, Treg depletion induced the formation of multiple clusters with Treg phenotypes (c5, c7, and c8) that now comprised ~50% of the total CD4 $T_{TS}$ cells (Figure 5F) that was not observed after CTLA4 blockade (Figure S6F). These tumor-specific iTregs expressed high levels of FoxP3, Helios, and CTLA4 (Figures 5F and 5G), with a subset expressing both CD69 and CD103 (Figure S6G), suggesting increased tissue homing/retention capacity. When compared with the Tregs in PBS-treated mice, the tumor-specific iTregs had increased expression of FoxP3 and multiple functional proteins (CD25, CD39, ICOS, CTLA4, and PDL1), Th1-associated proteins (SLAMF1, Blimp1, Tbet, and Tim3), but lack TCF1 and Bcl6, and did not express PD1 (Figures 5G, 5H, and S6H). This increased activation-protein expression was evident in the frequency of cells expressing these proteins and at the single-cell expression level in the tumor-specific iTreg (Figures 5H and S6H). Thus, Tregs rapidly induce and then maintain the CD4 $T_{TS}$ cell paralysis, and their depletion reciprocally promotes the differentiation of highly activated tumor-specific iTregs.

Mechanistically how CTLA4 and Tregs impair CD4 T cell proliferation in the dLN is unclear. Untreated CD4 $T_{TS}$ cells exhibit a transcriptional and metabolic profile consistent with sub-optimal activation. Indeed, depleting Treg or CTLA4 blockade specifically led to increased number and heightened activation of a specific population of DCs (a CD11b+ DC2 pop I) in the dLN, with elevated expression of the co-stimulatory molecules CD80 and CD86 (Figures S6I and S6J). Surprisingly, Treg depletion significantly increased MHC II expression on these cDC2 populations, whereas CTLA4 blockade did not (Figures S6I and S6J). These observations suggest that Tregs and CTLA4 synergistically induce T cell paralysis by limiting signals for T cell activation. Indeed, treating mice with aCD3 and/or aCD28 agonists antibodies successfully restored the proliferation of CD4 $T_{TS}$ cells in dLN (Figure 6A). Thus, the Treg- and CTLA4-mediated paralysis of CD4 $T_{TS}$ cells is overcome by increasing T cell activation signaling.

## Distinct effects of CTLA4 blockade and Treg depletion on tumor-specific CD4 T cell differentiation and programming

To distinguish how the signals from CTLA4 and Tregs regulate proliferation and differentiation of CD4 $T_{TS}$ cells, we depleted Tregs in combination with CTLA4 blockade. Blocking CTLA4 in combination with Treg depletion diminished the *de novo* iTreg differentiation (Figure 6B), indicating that CTLA4 signals on the CD4 $T_{TS}$ cells induce the iTreg differentiation when the suppression from Tregs is alleviated. In addition to reduced iTreg differentiation, the combination treatment significantly enhanced the production of IFN-γ, while slightly decreasing IL-2 and TNF-α production (Figures 6C and S6K). To understand the changes in cellular transcriptional networks underlying CTLA4- and Treg-mediated suppression of CD4 $T_{TS}$ cells, we performed scRNA-seq. Tumor-specific CD4 SMARTA T cells were isolated from the dLN on day 8 after PyMG initiation following: (1) isotype antibody treatment, (2) CTLA4 blockade, (3) Treg depletion, or (4) dual Treg depletion with CTLA4 blockade. Naive SMARTA cells were used for comparison. Seurat clustering revealed nine clusters across the conditions, with certain clusters emerging only following specific treatments (Figure 6D). Cell fate trajectory analyses revealed that c5 (the population that emerged only in CTLA4 blockade alone) and c3 (the population that emerged only in Treg depletion alone) are on the same differentiation pathway, whereas c6 (the population that emerged in dual treatment) had a distinct differentiation pathway (Figure 6E). Interestingly, the newly emergent clusters in the various treatment modalities all progress through c2 (Figure 6E), consistent with this being the initial path of differentiation that CD4 $T_{TS}$ cells are subsequently frozen in by CTLA4 and Tregs. Three minor clusters (c7–c9) each constituted less than 5% in each condition and their frequencies remained nearly unchanged after each treatment, therefore they were not included in further analysis. Naive SMARTA cells were composed of two similar populations based on their cluster defining genes (c1 and c4) with high levels of *Ccr7*, *Il7r*, and *Tcf7*, and therefore were combined in the future pathway analysis (Figure S7A). The majority of CD4 $T_{TS}$ cells in the dLN from isotype-treated mice formed a main c2 expressing a similar gene signature to our previous analysis (Figure 4B), such as high expression of *Izumo1r* (FR4), *Rgs10*, and *TCF7* (Figures 6D and S7A). Treg depletion led to an increase in iTreg (c3), characterized by *FoxP3* and *Ikzf2* (Helios) and other Treg-associated genes, such as *Tnfrsf4* (OX40) and *Ctla4* (Figures 6D and S7A), further confirming the iTreg differentiation. Blocking CTLA4 alone induced a unique c5 that, although it did not express the Treg-lineage-defining genes (*Foxp3, Ikzf2, Ctla4*), it shared many DEGs with the iTreg c3, including those involved in DNA transcription and repair, including *Hmgb2, Hmgn2*, and *Pclaf* (Figures 6D and S7A). The frequency of the iTreg c3 was reduced when blocking CTLA4 and depleting Tregs (in this case by ~20%), and a new c6 developed, characterized by high expression of genes associated with T cell activation and function, including *Fos, Fosb, Jun* (together forming the AP-1 complex),[37] *Nkg7* (lymphocyte granule exocytosis),[56] *Lag3*,[57,58] and *Eomes*[59] (Figure S7A), consistent with the CyTOF data demonstrating combination treatment promoting differentiation of highly activated CD4 $T_{TS}$ cells.

We next used IPA to perform pathway and upstream regulator analyses comparing c2 (the main cluster in isotype-treated mice) with the emergent clusters in each condition: c3 (the population that emerged only in Treg-depleted), c5 (the population that emerged

only in anti-CTLA4), and c6 (the population that emerged only in dual treatment). Among the top upstream regulators activated by either treatment alone are those associated with TCR and co-stimulation, including CD3, CD28, LCK, mTORC1, NF-κB complex, and PI3K complex (Figure S7B), thus further corroborating that both Treg and CTLA4 diminish antigen signaling to paralyze the CD4 $T_{TS}$ cells. The newly emergent cluster c3 after Treg depletion alone or c5 following CTLA4 blockade alone further elevated the OXPHOS metabolism pathway, particularly the TCA cycle, compared with isotype (Figures 6F and 6G); while IPA identified the glycolytic enzymes GAPDH and HK2 as upstream regulators even further inhibited (Figure S7B). Lipid biosynthesis, particularly cholesterol and triacylglycerol biosynthesis, is further promoted by CTLA4 blockade or Treg depletion alone, corresponding to inhibition of the PPAR pathway, regulating the efflux of cholesterol[35] (Figures 6F and 6G). In contrast, dual CTLA4 blockade and Treg depletion inhibited OXPHOS and cholesterol biosynthesis pathways and restored PPAR activity compared with the other conditions (Figures 6H and S7C). Thus, even though single treatments alone promoted proliferation (by enhancing T cell stimulation and likely through increased energy production), it exacerbated the reliance on OXPHOS and cholesterol biosynthesis, which are only corrected by the combination treatment. In addition to metabolic changes, the combination treatment also induced gene expression pathways that promote survival. Either CTLA4 blockade or Treg depletion alone exacerbated the activation of oxidative stress, as exemplified by the activation of upstream regulator pathways NRF2 and HIF1a, and pathways that negatively affect cell survival, such as necroptosis and senescence (Figures 6F, 6G, and S7B) that were already activated in untreated tumor-activated CD4 T cells (Figure 4F). In contrast, these pathways are inhibited in cells receiving dual treatment compared with the isotype sample (Figure 6H) or compared with the single treatment sample (Figure S7C). Thus, dual CTLA4 blockade and Treg depletion have combined effects to improve cellular metabolism, reduce oxidative stress, and promote survival and further differentiation.

## DISCUSSION

We demonstrate that dLN CD4 $T_{TS}$ cells are primed and begin to divide following tumor initiation. However, unlike CD8 $T_{TS}$ cells that continue to proliferate and infiltrate the tumor, the proliferation of CD4 $T_{TS}$ cells in the dLN is rapidly frozen in place shortly after the initial priming, stunting their differentiation and reducing their accumulation in the tumor. The paralysis is accompanied by gradual cell death over time, which would further limit the quality of the CD4 $T_{TS}$ cell response and suggest that early interventions that could amplify the response prior to attrition would be most beneficial. As a result, the help provided by CD4 $T_{TS}$ cells is rapidly limited and suboptimal for tumor control. Over time, a fraction of the paralyzed CD4 T cells are converted to iTregs in both the dLN and the tumor, suggesting that the tumors take advantage of the small amount of residual tumor-specific CD4 T cell differentiation to further promote their growth. The blunted proliferation and Th differentiation were actively maintained throughout tumor progression. Yet, CD4 $T_{TS}$ cells retained the ability to resume proliferation and differentiation when the suppressive constraints were abrogated either early or late in tumor progression, demonstrating that the tumor actively and continually suppresses CD4 T cells as a mechanism to promote

cancer cell growth. Overcoming the proliferative paralysis led to enhanced tumor control, elucidating the importance for the tumor to rapidly inhibit CD4 $T_{TS}$ cells during the early phase of cancer development.

Rather than being driven by heightened/prolonged antigenic stimulation and PD1:PDL1 interaction to induce functional exhaustion, CD4 $T_{TS}$ cell suppression is mediated at priming by multiple mechanisms that rapidly quell their activation (Figure S8). During priming, cooperative pathways are engaged to limit TCR and co-stimulatory molecule signaling at the level of the CD4 $T_{TS}$ cells and the APC, resulting in the paralyzed state. In the presence of Treg cells, DCs express lower levels of T cell-activating components, including MHC II and B7 family molecules. This is accompanied by the upregulation of CTLA4 on the CD4 $T_{TS}$ cells that further limits TCR signal and competes for binding to CD80 and CD86. Together, these collaborate to diminish T cell activation. Alleviating either of these inhibitors of T cell activation (or exogenously overcoming them with antibody-mediated antigenic stimulation) restored TCR signaling and co-stimulation to resume proliferation. However, depleting Tregs alone reciprocally induced highly activated tumor-specific iTregs to take their place. Interestingly, CTLA4 played a dual role. By itself it helped Tregs to inhibit TCR/co-stimulation signals to prevent proliferation. Then following Treg depletion, CTLA4 provided the signals to drive iTreg differentiation. Only by simultaneously limiting the constraints imposed by Tregs and CTLA4 could the differentiation of Th1 and Tfh cells be induced. It was interesting that the restricted CD4 Th differentiation included limited PD1 upregulation. PD1 blockade has been shown to minimally affect CD4 T cells in tumor models.[7] Moreover, only specific Th subsets may be amenable to anti-PD1-mediated functional restoration, while others remain insensitive to the therapy despite PD1 expression. For example, in chronic LCMV infection, despite high PD1 expression on all virus-specific CD4 T cells, anti-PD1 treatment enhanced CD4 Th1 and Treg cells, with only minimal effect on the dominant virus-specific Tfh population.[9] Thus, the low expression of PD1 and their uncommitted state (most closely resembling Tfh) may explain why PD1 blockade only has moderate affects to restore CD4 $T_{TS}$ cells compared with CD8 T cells, and instead preferentially enhances Treg responses in these cancer models.

The regulation of CD4 $T_{TS}$ cells occurred early within the dLN. CD4 $T_{TS}$ cells that did enter the tumor had fully diluted out their proliferation dye, suggesting that full proliferation is required for egress from the dLN to the tumor. Importantly, once in the tumor, the CD4 SMARTA $T_{TS}$ cells are phenotypically similar to that observed in human tumors. CTLA4 blockade and Treg depletion restored the proliferation of CD4 $T_{TS}$ cells in the dLN, and again in this situation, the CD4 $T_{TS}$ cells that infiltrated the tumor had completely diluted proliferation dye. This is consistent with clinical observations and mouse models that immune-checkpoint blockades induce new T cell clones previously not observed within the tumor.[60] Our study provides an explanation for this observation. CD4 $T_{TS}$ cells are present at very low levels in the dLN and tumor due to their restricted proliferation. By expanding CD4 $T_{TS}$ cells from low levels in the dLN, immunotherapy enables their homing to the tumor where they can become identifiable clones. Thus, regarding CD4 T cells, immunotherapy may induce the priming and activation of new tumor-specific CD4 T cells, for example against neo-antigens, but we show that it can also reactivate and expand low amounts of pre-existing clones to home to the tumor. It is also important to note that our

study mostly examines a single antigen-specific CD4 T cell epitope, which may explain why the overall level of tumor infiltration is so small in our model. If there is a little infiltration from multiple antigen epitope-specific responses, then the total number of tumor-specific CD4 T cells in the tumor would cumulatively increase. However, for any single epitope-specific response, the infiltration would be small, especially compared with CD8 T cells.

Metabolically, the paralyzed CD4 T cells exhibited reduced ability to utilize glucose and glycolysis pathways compared with fully differentiated virus-specific Th1 and Tfh cells. Instead, tumor-activated CD4 T cells heavily favor OXPHOS (based on transcriptome and protein expression), with particularly elevated proteins involved in the TCA cycle, and glutamine metabolism whose products directly fuel into the TCA cycle. Recent studies have shown the importance of TCR and CD28 signals in inducing metabolic reprogramming and inducing aerobic glycolysis to fuel robust proliferation and differentiation,[61] further explaining why the paralysis limits CD4 $T_{TS}$ cells. The CD4 $T_{TS}$ cells also exhibited reduced expression of important mitochondrial proteins, suggesting impaired mitochondria function and further limited ability to generate ATP. Recent evidence indicates metabolic regulation of T cells in the TME (limited glucose and glutamine, an increased hypoxic environment) as an important mechanism inhibiting T cell activity, leading to reduced function and exhaustion.[62] Our study now indicates that the metabolic fitness of CD4 $T_{TS}$ cells is programmed early in the dLN, as opposed to the tumor itself,[63] although the TME likely further contributes to the function and differentiation of CD4 $T_{TS}$ cells when they arrive. Interestingly, CTLA4 blockade or Treg depletion by themselves further reinforced the metabolism present in untreated CD4 $T_{TS}$ cells, suggesting that resuming the proliferation is not necessarily accompanied by correction of metabolism. Specifically, OXPHOS potential was further enhanced, along with an increase in proteins involved in cholesterol and fatty acid biosynthesis and the further inhibition of PPAR activity. Increased cellular cholesterol is associated with the differentiation of Tregs,[64] providing a potential link to how Treg depletion or CTLA4 blockade both increased transcriptomic changes favoring iTreg induction. Altogether, our study demonstrates that suboptimal priming (inadequate TCR and CD28 signals) of CD4 $T_{TS}$ cells in the dLN early during cancer development promotes a paralyzed state, characterized by defects in proliferation, differentiation, and metabolism that promote tumor growth.

## Limitations of the study

Our study identifies a tumor-mediated T cell dysregulation that specifically inhibits the generation of CD4 $T_{TS}$ cell response in the dLN. This defect, referred to as paralysis, represents a distinct state from T cell exhaustion and contributes to the failure of long-term tumor control by the immune system. One limitation of this study is its scope of application in human cancers. Although we identified human CD4 T cells in patient dLNs expressing similar transcriptomic, further functional assays are required to demonstrate whether these human T cells also exhibit proliferative and differentiative paralysis. Further, longitudinal studies in humans would be needed to determine how and when T cell paralysis occurs in the dLN, and to further access its impact on disease progression and immunotherapy. In addition, our study reports that, in the absence of Tregs, mouse CD4 $T_{TS}$ cells are rapidly

pushed toward an iTreg phenotype by their own expression of CTLA4, particularly when other Tregs are deleted. It remains to be determined whether human CD4 $T_{TS}$ cells undergo a similar process in patients, particularly in response to Treg-depleting approaches.

# STAR★METHODS

## RESOURCE AVAILABILITY

**Lead contact—**Further information and requests for resources and reagents should be directed to and will be fulfilled by the lead contact, David Brooks (dbrooks@uhnresearch.ca).

**Materials availability—**Further information and material requests should be addressed to David Brooks (dbrooks@uhnresearch.ca).

### Data and code availability

- This paper does not report original code.

## EXPERIMENTAL MODEL AND SUBJECT DETAILS

**Mice—**For all experiments, female mice were used for breast cancer cell lines (PyMT and PyMG) and either female or male mice were used for B16-F10 and colorectal carcinoma (MC38 and MC38GP). C57BL/6 mice (7–12 weeks old) were purchased from Princess Margaret Cancer Center or The Jackson Laboratory. LCMV-$GP_{61–80}$-specific CD4 TCR transgenic (SMARTA; CD45.1+) mice and LCMV-$GP_{33–41}$-specific CD8 TCR transgenic (P14; CD45.1+) were described previously.[68] OT-II mice (Stock No: 004194) were purchased from The Jackson Laboratory. CD4KO (Stock No: 002663) and FoxP3-DTR (Stock No: 016958) breeders were purchased from The Jackson Laboratory and maintained in the mice facility at Princess Margaret Cancer Center. $\beta_2$m−/− female mice (Stock No:002087) were purchased from The Jackson Laboratory and used for harvesting bone marrow. CTLA4 flox/flox mice were provided by Dr. Pamela Ohashi (University health Network) and crossed to $FoxP3^{eGFP–Cre-ERT2}$ (Jackson stock No: 016961). All mice were housed under specific pathogen-free conditions. Mouse handling conformed to the experimental protocols approved by the OCI Animal Care Committee at the Princess Margaret Cancer/University Health Network.

**T cell adoptive transfer, TAGIT labeling and cell proliferation quantification—**CD4 SMARTA T cells, CD4 OT-II T cells or CD8 P14 T cells were isolated from the spleens of transgenic mice using EasySep mouse naive CD4 T cell negative isolation kit (Catalog No. 19852, STEMCELL) or EasySep mouse naive CD8 T cell negative isolation kit (Catalog No. 19858, STEMCELL), respectively. For tumor experiments, 100,000 SMARTA, OT-II or P14 T cells were transferred to mice i.v. via retro-orbital sinus one to two days prior tumor injection. For LCMV experiments, 3,000 SMARTA cells were transferred to mice i.v. via retro-orbital sinus one to two days prior infection.Where indicated, transgenic T cells were labeled with Tag-it Violet Proliferation and Cell Tracking Dye (Cat No. 425101 Biolegend). The frequency of SMARTA cells that proliferated during culture was determined as described by Gett et al.[69] Briefly, the number of cells in each division peak

was divided by $2^i$ (where i equals the number of divisions), and the resulting number of each division was then summed as the number of SMARTA cells that had divided. This number was then divided by the sum of the divided SMARTA and the number of undivided cells. This number was then expressed as the percentage of proliferation.

**LCMV infection—**For experiments where LCMV was used as control, mice were infected with 2 million plaque-forming units (PFU) of LCMV-Cl13 i.v. via the retro-orbital sinus, or two hundred thousand PFU. of LCMV-Armstrong intraperitoneally (i.p.) into mice. Virus stocks were prepared and viral titers were quantified as described previously.[68] LCMV-specific $CD4^+$ SMARTA T cells were isolated from the spleens of transgenic mice as described above. Then 3,000 CD45.1+ SMARTA cells (donors) were transferred i.v. into the retro-orbital sinus of naive CD45.2 + C57BL/6 mice (recipients) that were then infected with LCMV-Cl13 or -Armstrong one day later. Spleen cells were used for analysis of virus-specific CD4 T SMARTA cells.

**Tumor cell lines and LCMV-GP1–100 vector construction—**PyMT and MC38OVA cell line were provided by Dr. Pam Ohashi (University Health Network). The MC38 tumor line was provided by Dr. Daniel De Carvalho (University Health Network). B16-F10 and MC38OVA was provided by Dr. Tracy McGaha (University Health Network).

To generate PyMG cell line, LCMV-$GP_{1–100}$ was cloned into MSCV-IRES-Thy1.1 DEST vector[70] (MSCV-IRES-Thy1.1 DEST was provided to Addgene by Dr. Anjana Rao, Addgene plasmid# 17442; http://n2t.net/addgene:17442; RRID:Addgene_17442) using TaKaRa In-Fusion HD Cloning Plus kits (Cat# 638917) to get MSCV-LCMVGP-IRES-Thy1.1 vector. The following primers were used to amplify LCMV-$GP_{1–100}$ and perform infusion cloning, forward primer: CGCCGGAATTAGATCATGGGTCAGATTGTGACAAT; reverse primer: ACCGGATCCAGTCGATCAGTAATGGTGGGAGTTGTT. Then MSCV-LCMVGP-IRES-Thy1.1 vector and pCL-ECO vector[71] (pCL-Eco was provided to Addgene by Dr. Inder Verma, Addgene plasmid# 12371; http://n2t.net/addgene:12371; RRID:Addgene_12371) were transfected in 293 T cells with lipofectamine 3000 (Cat# L3000001, Thermo Fisher) to generate virus for transfection. The parental PyMT cell line was then transfected with the pseudotyped LCMV-GP1–100 containing virus (MOI = 1) in the presence of polybrene. After viral transfection, single Thy1.1+ tumor cells were isolated by FACSorting and single cell clones generated. PyMG was selected among a tested single cell clones after injecting and tracking their growth in female C57BL/6 mice.

Transposon transduction was used to generate the MC38GP cell line. LCMV-$GP_{1–100}$-Thy1.1 sequence was amplified from MSCV-LCMVGP-IRES-Thy1.1 vector using the following primers: forward: GCCTCTGAGGCCACCATGGGTCAGATTGTGACAATGTTTG; reverse: ATTGATCCCCAAGCTTCACAGAGAAATGAAGTCCAGGGC, and then cloned into pSBbi-Pur vector[72] (pSBbi-Pur was a gift from Eric Kowarz, Addgene plasmid # 60523; http://n2t.net/addgene:60523; RRID:Addgene_60523) using TaKaRa In-Fusion HD Cloning Plus kits (Cat# 638917) to get pSBbi-Pur-LCMVGP-Thy1.1 vector. Then pSBbi-Pur-LCMVGP-Thy1.1 vector and pCMV(CAT)T7-SB100[73] (pCMV(CAT)T7-SB100 was a gift from Zsuzsanna Izsvak, Addgene plasmid # 34879; http://n2t.net/addgene:34879;

RRID:Addgene_34879) were transfected into MC38 cell line with lipofectamine 3000 (Cat# L3000001, Thermo Fisher). Thy1.1+ tumor cells were then FACs sorted into single cell clones and grown with puromycin (8ug/ml, Gibco Ref A1113803) selection media. MC38GP was selected based on the growth rate in male and female C57BL/6 mice.

**Tumor cell injection—**For injection of PyMT and PyMG, tumor cells were washed thoroughly with PBS after trypsinization and resuspended at $1 \times 10^6$ cells per 20μL in PBS. Female mice received 20μL injection at the left lower $5^{th}$ mammary fat pad to avoid injection into nearby lymph node. For injection of MC38, MC38GP, MC38OVA and B16-F10, tumor cells were resuspended at $2 \times 10^5$ per 50ul PBS. Female or male mice received 50ul injection at the inner side of the leg. Inguinal lymph nodes were tumor draining lymph nodes for all tumors used.

**Tissue processing—**Tumors were harvested and manually dissociated into small pieces in gentleMACS C tubes (Miltenyi Biotec) with 5mL RPMI 1640 medium with 100U/ml Collagenase I (Thermofisher 17100017) and 10ug/ml DNase I (Sigma DN25–1G) and 2% FBS. For PyMG/PyMT tumors, protocol 37_m_TDK_2 of the gentleMACS Dissociator (Miltenyi Biotec, 130–095-937) was used. For B16 and MC38/MC38GP, protocol 37_m_TDK_1 was used. Single cell suspensions were obtained by filtering through pre-separation filters (70μm) (Miltenyi, order#130–095-823). Due to the limitation of the number of live cells recovered from day 8 tumor, all flow plots concerning day 8 TME was collected by combing individual tumor samples of each group into one sample during digestion. Inguinal lymph nodes were harvested and manually dissociated into small pieces in 1.5mL centrifuge tubes with 400ul buffer I (RPMI with 10% FBS and 1% HEPES), followed by digestion with 1 mg/ml Collagenase IV from Clostridium histolyticum (C5138 Sigma) and 0.15 mg/ml DNase I (Sigma) at 37° for 30 min. Lymph node single cell suspension was obtained by filtering through the strainer snap cap of Falcon 352235 round-bottom polystyrene test tubes (Fisher scientific Cat#08–771-23). Spleens were harvested from LCMV infected mice and manually dissociated into single cell suspension with a tissue smasher.

***In vitro* generation and peptide labeling of bone marrow derived dendritic cells—**bmDCs were generated as previously described.[74] Briefly, $2 \times 10^6$ bone marrow cells were cultured at 37°C in 10mL bmDC culture medium (RPMI 1640 medium with 10% FBS, penicillin/streptomycin and 2-Mercaptoethanol) with 40 ng/mL GM-CSF (BioLegend). At day 3, 10 mL fresh bmDC culture medium with 40 ng/ml GM-CSF was added. At day 6 and 8, 10mL media was removed and replaced with fresh bmDC culture medium with 20 ng/ml (day 6) or 10 ng/ml (day 8) GM-CSF and 20 ng/ml IL-4. Loosely adherent cells were harvested at day 10 and stimulated with 1 μg/mL LPS (Sigma-Aldrich) in 37°C incubator for 24 h. Cells were then pulsed with 5 μg/ml of LCMV-$GP_{61–80}$ peptides or left un-pulsed in bmDC culture medium for 2 h at 37°C incubator. One million bmDCs were injected per mouse intravenously on the same day as tumor injection.

***In vivo* antibody blockade, diphtheria toxin and tamoxifen treatments—**For *in vivo* CTLA4 blockade, 300 μg/mouse of anti-CTLA4 (Clone UC10–4F10–11, BioXcell

Cat# BE0032) or isotype (polyclonal Armenian Hamster IgG, clone: NA, BioXcell Cat#BE0091) antibodies were administered intravenously at day 0, 2 and 5 after tumor injection for early treatment and day 21, 23 and 26 for late treatment. For PDL1 blockade, 250μg antibodies (Clone 10 F.9G2, BioXcell Cat#BE0101) or isotype control (rat IgG2b Clone LTF-2, BioXcell, Cat#BE0090) were administrated i.v. at day 0, 2 and 5 following tumor injection. 500μg/mouse anti-CD25 (clone PC-61.5.3, BioXcell, Cat# BE0012) *in vivo* depleting antibodies or isotype (Rat IgG1, clone HRPN, BioXcell Cat#BE0088) were administrated at day −4 and −2, and depletion efficiency was confirmed with blood by Flow Cytometry. For CD28 agonist, 100μg/mouse anti-CD28 (clone PV-1, BioXcell, Cat#BE0015–5) or isotype (polyclonal Armenian hamster Armenian Hamster IgG, clone N/A, BioXcell, Cat#BE0091) antibodies were administrated at day 5 post tumor injection. For CD3 agonist, 100μg/mouse anti-CD3 (clone 145–2C11, BioXcell, Cat#BP0001–1) or isotype (polyclonal Armenian Hamster IgG, clone N/A, Cat#BP0091, BioXcell) antibodies were administrated at day 5 post tumor injection. For diphtheria toxin (DT)-mediated Treg depletion *in vivo*, 0.5μg DT was dissolved in 100ul PBS and administered retro-orbital at day 0 and 2 after tumor injection. Depletion of Tregs was confirmed via blood. For tamoxifen-mediated CTLA4 deletion, FoxP3-Cre x CTLA4 flox mice were treated daily for 5 days before tumor injection intraperitoneally with freshly made tamoxifen (2mg/mouse per treatment). Deletion of CTLA4 was confirmed by flow cytometric staining in blood.

**Flow cytometry and *ex vivo* peptide stimulation—**Single-cell suspensions were prepared from organs and were stained *ex vivo* using antibodies in. Transcription factor stains were performed using FoxP3 Transcription Factor kit (eBiosciences, Cat No 00–5523-00). Samples were run on a FACS Verse or a FACS Lyric (BD Biosciences) and data analyzed using Flow Jo software (v.10; Treestar). For *ex vivo* peptide stimulation and cytokine staining, LN single cell suspension were stimulated for 5h at 37°C with 5ug/ml of LCMV-$GP_{61–80}$ in the presence of 50 U/ml recombinant murine IL2 (Thermofisher P2747) and 1 mg/ml Brefeldin A (Sigma). Cells were then stained with Zombie Aqua Fixable Viability Kit (BioLegend), followed by extracellular staining. The cells were then washed, fixed, permeabilized (BioLegend cytokine staining kit) and stained with anti-cytokine antibodies.

**CRISPR-mediated CTLA4 deletion—**CD4 SMARTA T cells were isolated from naive mice and were washed and resuspended in 20 μL buffer P3 (P3 Primary Cell 4D-Nucleofector X Kit S, Lonza, cat. no. V4XP-3032). Between $10^5$ to $10^7$ cells were used per nucleofection. Single guide RNAs (sgRNAs) were incubated together with recombinant Cas9 (TrueCut Cas9 Protein v2, 5ug/ul, Thermo Fisher Scientific, cat. no. A36499) for 15 min at room temperature, at a ratio of 1:3.3 (i.e., 30 pmol Cas9 protein per 100 pmol sgRNA) to form the CRISPR–Cas9–sgRNA-ribonucleoprotein (RNP) complex. To increase deletion efficiency, a combination of three different pre-validated sgRNAs against CTLA-4 were mixed with the cell suspension (see list below), and transferred into a 16-well nucleocuvette strip (Lonza, cat. no. V4XP-3032). For negative control, sgRNA (TrueGuide sgRNA Negative Control, non-targeting 1; Thermo Fisher Scientific, cat. no. A35526t) was annealed with Cas9 at the same molar ratio. Cells were nucleofected using program DS137 and buffer P3 on the 4D-Nucleofector system (4D-Nucleofector X unit, Lonza, cat. no.

AAF-1003X). Pre-warmed complete culture medium supplemented with IL-7 (10 ng/ml) was added to each well and cells were transferred to a 96-well plate for recovery at 37°C for 6 h before TAGIT label and transfer to mice that subsequently received tumor cells. The knockout efficiency based on CTLA-4 expression was confirmed by flow cytometry.

**sgRNA sequences against mouse CTLA-4 - TrueGuide synthetic sgRNA (Thermo Fisher Scientific)—**CRISPR58571_SGM.

| **Target DNA sequence** | **TGGCTTGTCTTGGACTCCGG** |
|---|---|
| PAM Sequence | AGG |
| Target locus | Chr.1: 60909172–60909194 on GRCm38 |
| Strand | Forward |
| Application | Gene Knockout |
| | Exon 1 |

CRISPR58590_SGM.

| **Target DNA sequence** | **GGGACTGTACCTCTGCAAGG** |
|---|---|
| PAM Sequence | TGG |
| Target locus | Chr.1: 60912685–60912707 on GRCm38 |
| Strand | Forward |
| Application | Gene Knockout |
| | Exon 2 |

CRISPR58569_SGM.

| **Target DNA sequence** | **GACCCAACCTTCAGTGGTGT** |
|---|---|
| PAM Sequence | TGG |
| Target locus | Chr.1: 60912433–60912455 on GRCm38 |
| Strand | Forward |
| Application | Gene Knockout |
| | Exon 2 |

**Time-of-flight mass cytometry (CyTOF)—**CyTOF antibodies are listed in. Where indicated in, already conjugated antibodies were purchased from Fluidigm. Conjugation of purified antibodies was performed at the SickKids-UHN Flow and Mass Cytometry Facility using the MaxPar Antibody Labeling Kit (Fluidigm). All antibodies were titrated prior to the experiments. CD4 T cells were enriched with autoMACS Pro Separator (Miltenyi Biotec) using CD4 (L3T4) microbeads (order no. 130–117-043, Miltenyi Biotec).

For T cell phenotype panel: Samples were washed with PBS and stained with 12.5μM cisplatin (Cedarlane/biovision 1550–1000) in PBS for 1 min at room temperature before quenching with FBS. Samples were stained for 15 min at room temperature with FcR blockade and with antibodies that did not stain well after fixation (labeled in red in Tables). Cells were fixed and permeabilized for 10 min at room temperature with Transcription Factor Staining Kit (eBioscience, Cat No 00–5523-00), and then barcoded with Cell-ID 20-Plex Pd Barcoding Kit (Fluidigm, Product No 201060). Combined samples were then incubated with surface antibody cocktail () for 30 min at 4°C. After surface staining, samples were permeabilized and stained with intracellular antibodies for 30 min at room temperature using Transcription Factor Staining Kit (eBioscience, Cat No 00–5523-00). For the DNA stain, cells were incubated overnight in PBS (Multicell) with 0.3% (w/v) saponin, 1.6% (v/v) paraformaldehyde (Polysciences Inc.), and 1nM iridium (Fluidigm). Samples were acquired on a Helios mass cytometer (Fluidigm) at Sick Kids – UHN Flow and Mass Cytometry Facility or Princess Margaret Cancer Center. EQ Four Element Calibration Beads (Fluidigm) were used to normalize signal intensity over time on CyTOF software version 6.7. FCS files were manually debarcoded and analyzed using R as described below.

For metabolism panel: Cells were washed with PBS and samples were labeled with 103Rh viability dye (for live/dead cell discrimination) at 37°C for 15min, followed by washing with PBS. Samples were then fixed and barcoded as described above. Following Fc receptor blocking for 10 min at room temperate, the pooled barcoded sample was incubated with the first surface cocktail of CD36-FITC and CD98-APC for 30 min at 4°C followed by washing. The cells were then stained with a second surface cocktail () for 30 min at 4°C. The sample was stained with intracellular antibody staining for 30 min at room temperature. The DNA stain was then performed as described above.

**Bioinformatic analyses (CyTOF)—**Data pre-processing and dimensionality reduction of CyTOF data: Preprocessing of files was performed using FlowJo Software (v10) software. Samples were manually debarcoded and exported as separated FCS files. SMARTA cells were filtered by gating on DNA, singlets, live cells and CD45.1+ CD45.2− $CD4^+$ MHCII− TCRβ+ cells, and raw signal events were then exported as matrices in csv format. Data was then analyzed in R (v 4.1.0). All events were included in dimensionality reduction. Marker expression values were arcsinh transformed using a custom co-factor for each marker before clustering. Phenograph and UMAP were performed using the R implementation of the “Rphenograph” package (v 0.99.1) by JinmiaoChen lab on github[66] (https://github.com/JinmiaoChenLab/Rphenograph) and package “umap” (v 0.2.7.0). Differential state and abundance analyses were performed by “diffcyt” package[19] (v 1.14.0).

**Metabolic pathway scoring:** First, the sum of arcsinh-transformed expression of enzymes were calculated on a single cell level for each metabolic pathway (markers used to evaluate each pathway are defined as following), and then divided by the number of enzymes used to evaluate each metabolic pathway:

Glycolysis: GLUT1, HK2, GAPDH, MCT4.

Glutamine and amino acid: CD98, GLS, GOT2, GLUD1/2.

OXPHOS: IDH1, CS, ATP5A, CytC.

Lipid: CD36, CPT1A, ACADM, pACC.

Statistical significance of each pathway was calculated at the single cell level in R using Wilcox test only comparing between CD4 $T_{TS}$ cells to Th1 and Tfh.

**Single cell RNA-sequencing—**SMARTA cells were transferred into WT or FoxP3-DTR mice one day prior to tumor injection. Mice were treated with DT or PBS at day 0 and 2 post PyMG tumor injection. Anti-CTLA4 antibody was injected at day 0, 2 and 5 after tumor injection. Mice were sacrificed at day 8 and inguinal lymph nodes were harvested and digested into single cell suspension. CD4 T cells were enriched on autoMACS Pro Separator (Miltenyi Biotec) with CD4 positive selection beads (clone L3T4, Order no. 130–117-043, Miltenyi Biotec), followed by FACSorted on a Moflo Astrios (Beckman Coulter) or a BD FACSaria Fusion cell sorter for SMARTA cells based on CD45.1 expression. After sorting and purity check on flow cytometer, SMARTA cells were then resuspend in 10X Genomics Chromium single cell RNA master mix and loaded onto a 10x chromium chip. cDNA Library was generated using the Chromium Single Cell 3′ Reagents Kits v2 User Guide:CG00052 Rev B, and then sequenced on the Illumina HiSeq 2500 platform to achieve an average of 40,000 reads per cell. Sequencing was performed at the Princess Margaret Genomics Center. TAGIT expression on SMARTA cells were checked before and after sorts to make sure the procedures did not preferentially kill the effector population.

### Bioinformatic analyses (mouse scRNA-Seq)

**Reads alignment and quantification:** Base calling was performed using Illumina RTA (v 3.4.4) and bcl2fastq2 (v 2.20) to generate bcl files. Cell ranger (v 6.0.0) was then used to demultiplex bcl into fastq files and to align reads to the mm10 genome (refdata-gex-mm10–2020-A downloaded from the 10x genomics website).

### Data preprocessing

**Quality control and normalization:** Data was further analyzed using R (v 4.1.1) and the R Seurat (v 4.0.4) package (Hao et al. 2021). Cells meeting the below criteria were considered as good quality cells and were kept for subsequent analyses.

- Naive: 500 < genes expressed <2300 and mitochondrial genes (%) < 10 (7955 cells)
- Isotype: 500 < genes expressed <6000 and mitochondrial genes (%) < 12 (1099 cells)
- aCTLA4: 1000 < genes expressed <6000 and mitochondrial genes (%) < 7 (4566 cells)
- Treg depletion: 700 < genes expressed <7000 and mitochondrial genes (%) < 12 (2186 cells)
- Treg depletion + aCTLA4: 600 < genes expressed <6000 and mitochondrial genes (%) < 13 (4343 cells).

Genes expressed in less than 3 cells and more than 12,000 cells were excluded from further analyses. Gene expression of all samples were initially normalized using the LogNormalize method and adjusted to regress out percentage of mitochondrial genes and cell cycle genes. Then data was exported to the SeqGeq application (v 1.8) where raw counts were normalized using the scTransform normalization and clustered using Louvain algorithm and the resolution indicated in the respective figure legends using the Seurat plug-in (4.0.4)[67] of SeqGeq.

**Gene set variation analysis (GSVA):** We estimated activity of Hallmark gene sets taken from MSigDB (PMID: 23323831 and 21546393) on cellular level using the GSVA (v 1.40.0) and msigdbr (v 7.4.1) R packages and the R project (v 4.1.1) with the following parameters: kcdf = “Poisson”, method = ‘gsva’, min.sz = 5, max.sz = 500, parallel.sz = 13. Enrichment scores for each cluster were then calculated as the average gsva scores of cells in each cluster. A two-sided Mann Whitney U test was performed to test whether gsva scores of celles in each cluster are significantly different than those in cells belonging to the remaining clusters. P-values were then corrected for multiple hypotheses testing using the FDR method. Gene sets having an FDR <0.05 for at least one cluster were retained.

**Monocle trajectory analysis:** To determine cell trajectory, we used monocle3 (v 1.0.0) R package with R (v 4.1.1) (PMID: 24658644). Seurat clusters were used for this analysis. Graph was learnt using learn_graph_control = list(ncenter = 170) for the isotype sample and ncenter = 260 for all samples. Cells were ordered and pseudotime was calculated using default parameters.

**Venn diagrams:** First, 6 differential expression analyses were performed between (1) paralyzed CD4 $T_{TS}$ cells vs. naive CD4 T cells, (2) effector virus-specific CD4 T cells vs. naive CD4 T cells, (3) exhausted virus-specific CD4 T cells vs. naive CD4 T cells, (4) paralyzed CD4 $T_{TS}$ cells vs. naive CD8 T cells, (5) effector virus-specific CD8 T cells vs. naive CD8 T cells, (6) exhausted virus-specific CD8 T cells vs. naive CD8 T cells. The top 500 up-regulated genes of the first 3 analyses make the left panel and the top 500 up-regulated genes of the last 3 analyses make the right panel in Figure 4E. Each dataset was first compared to naive cells to identify differentially expressed genes (DEGs) unique to each T cell population, separate from “general” T cell expressed genes. The different datasets were procured from: scRNA-seq data for effector virus-specific CD4 T cells[52]; exhausted virus-specific CD4 T cells[53]; naive virus-specific CD8 T cells[51]; effector virus-specific CD8 T cells[51] and exhausted virus-specific CD8 T cells.[51]

**GSEA and IPA:** *Gene Set Enrichment Analysis*[75,76] was performed by GSEA application (Broad Institute v. 4.2.2) using the Enrichment Map gene sets from ImmuneSigDB “GSE14308_TH17_VS._NAIVE_CD4_T cell_UP”[77] (for Th17), “GSE14308_TH2_VS._NAIVE_CD4_T cell_UP”[77] (for Th2), “GSE14415_INDUCED_TREG_VS._TCONV_UP”[78] (for iTreg), and Th1 and Tfh gene sets generated in previous Brooks Lab project.[9] Gene lists were generated and exported from SeqGeq and preranked based on p value in R using the formula sign(log(gene.list$FoldChange))*(−log10(gene.list$p value)).

Ingenuity Pathway Analysis software (Qiagen) was used for the predicted pathway and upstream regulator analysis based on the gene lists generated from SeqGeq.

**Human scRNA-Seq data analyses—**scRNA-Seq data was taken from two previously published studies of breast[54] (GEO: GSE180286) and lung adenocarcinoma[55] (GEO: GSE131907) cancers; data was reanalyzed from scratch as described below.

**Breast cancer:** samples were obtained from lymph nodes of 5 breast cancer patients (2 biological replicates from each patient), one of these samples (P3_LN1) was considered an outlier, as it has, on average, more expressed genes, read counts and mitochondrial genes percentage per cell than all other samples, so it was excluded from further analyses. Lung cancer: samples were obtained from lymph nodes of 17 lung cancer patients.

We filtered out dead and poor-quality cells and doublets by excluding cells meeting the following criteria: nFeature_count <200, nFeature_count > nFeature_count_cutoff, mitochondrial genes (%) > mitochondrial_percentage_cutoff for each sample. Cutoffs were chosen in a way to remove the cells at the upper tail of the nFeature_count and mitochondrial_percentage distributions. Used cutoffs and number of cells before and after filtering can be found in Table S1.

We used Seurat (v 4.3.0) and R (v 4.2.2) to merge and logNormalize samples of each cancer type apart. All samples were then integrated using the STACAS (v 2.0.2) algorithm using default parameters (PubmedID: 32845323). After integration of all samples together, we scaled data, ran UMAP using the first 26 principal components, ran FindNeighbors and ran FindClusters using resolution 0.3. Next, T cells were identified based on CD3E and TRAC expression profiles as cells in clusters: 0, 1, 3 and 6. Data was then re-clustered with resolution 0.8, and CD4 T cells. Subsequently, we re-clustered cells using resolution 0.8 and identified CD4 T cells by annotating cells using SingleR (2.0.0) (used parameters: de.method = “wilcox”, sd.thresh = 1.2) and Monaco (GSE107011) as a reference dataset (Pubmed ID: 30726743) on cluster level (resolution 0.8) and obtained 55,521 CD4 T cells. To identify paralyzed CD4 T cells in human, we considered the 373 genes in Figure 4G (left panel, genes in blue circle) as a signature of the tumor-specific CD4 paralyzed in mouse and used their orthologs in human to identify similar cells in human. To this end, we used the cosine similarity applied on 1) mean expression of the 373 genes in mouse and their human orthologs in each cell of the 55,521 cells in human. Mouse to human orthologs mapping was taken from MGI reports (http://www.informatics.jax.org/downloads/reports/). Human paralyzed CD4 T cells were identified by cells having a $Z$ score of cosine similarity >2.5, resulting in 616 cells. We then defined a signature of human paralyzed CD4 T cells as the average expression of the top 25 up-regulated genes in human paralyzed CD4 T cells to all other CD4 T cells in human samples using the findMarkers function of Seurat. The Signature Expression was quantified in each cell as the Sum(normalized expression of gene1, gene2 … gene25)/25. Finally, we performed biological processes GO enrichment analysis using gProfileR (PubmedID: 31066453) with default parameters, except that we treated the list of 25 genes as an ‘ordered query’.

**Statistical analyses (other than CyTOF and scRNAseq)—**Mann-Whitney U test or two-way ANOVA were calculated by GraphPad Prism 9 (GraphPad Software, Inc.).

## Supplementary Material

Refer to Web version on PubMed Central for supplementary material.

## ACKNOWLEDGMENTS

We thank past and present members of the Brooks laboratory for technical help and discussion. This work was supported by the Canadian Institutes of Health Research (CIHR) Foundation grant FDN148386 (to D.G.B.), the National Institutes of Health (NIH) grant AI085043 (to D.G.B.), and the Scotiabank Research Chair to D.G.B.

## REFERENCES

1. Waldman AD, Fritz JM, and Lenardo MJ (2020). A guide to cancer immunotherapy: from T cell basic science to clinical practice. Nat. Rev. Immunol. 20, 651–668. [PubMed: 32433532]
2. Pauken KE, and Wherry EJ (2015). Overcoming T cell exhaustion in infection and cancer. Trends Immunol. 36, 265–276. [PubMed: 25797516]
3. Hunder NN, Wallen H, Cao J, Hendricks DW, Reilly JZ, Rodmyre R, Jungbluth A, Gnjatic S, Thompson JA, and Yee C (2008). Treatment of metastatic melanoma with autologous CD4+ T cells against NY-ESO-1. N. Engl. J. Med. 358, 2698–2703. [PubMed: 18565862]
4. Tran E, Turcotte S, Gros A, Robbins PF, Lu YC, Dudley ME, Wunderlich JR, Somerville RP, Hogan K, Hinrichs CS, et al. (2014). Cancer immunotherapy based on mutation-specific CD4+ T cells in a patient with epithelial cancer. Science 344, 641–645. [PubMed: 24812403]
5. Ahrends T, Spanjaard A, Pilzecker B, Ba¸ ba1a N, Bovens A, Xiao Y, Jacobs H, and Borst J (2017). CD4+ T Cell Help Confers a Cytotoxic T Cell Effector Program Including Coinhibitory Receptor Downregulation and Increased Tissue Invasiveness. Immunity 47, 848–861.e5. [PubMed: 29126798]
6. Cui C, Wang J, Fagerberg E, Chen PM, Connolly KA, Damo M, Cheung JF, Mao T, Askari AS, Chen S, et al. (2021). Neoantigen-driven B cell and CD4 T follicular helper cell collaboration promotes anti-tumor CD8 T cell responses. Cell 184, 6101–6118.e13. [PubMed: 34852236]
7. Wei SC, Levine JH, Cogdill AP, Zhao Y, Anang NAAS, Andrews MC, Sharma P, Wang J, Wargo JA, Pe'er D, and Allison JP (2017). Distinct Cellular Mechanisms Underlie Anti-CTLA-4 and Anti-PD-1 Checkpoint Blockade. Cell 170, 1120–1133.e17. [PubMed: 28803728]
8. Brooks DG, Teyton L, Oldstone MBA, and McGavern DB (2005). Intrinsic functional dysregulation of CD4 T cells occurs rapidly following persistent viral infection. J. Virol. 79, 10514–10527. [PubMed: 16051844]
9. Snell LM, Xu W, Abd-Rabbo D, Boukhaled G, Guo M, Macleod BL, Elsaesser HJ, Hezaveh K, Alsahafi N, Lukhele S, et al. (2021). Dynamic CD4+ T cell heterogeneity defines subset-specific suppression and PD-L1-blockade-driven functional restoration in chronic infection. Nat. Immunol. 22, 1524–1537. [PubMed: 34795443]
10. Oxenius A, Fidler S, Brady M, Dawson SJ, Ruth K, Easterbrook PJ, Weber JN, Phillips RE, and Price DA (2001). Variable fate of virus-specific CD4(+) T cells during primary HIV-1 infection. Eur. J. Immunol. 31, 3782–3788. [PubMed: 11745399]
11. Fahey LM, Wilson EB, Elsaesser H, Fistonich CD, McGavern DB, and Brooks DG (2011). Viral persistence redirects CD4 T cell differentiation toward T follicular helper cells. J. Exp. Med. 208, 987–999. [PubMed: 21536743]
12. Snell LM, Osokine I, Yamada DH, De la Fuente JR, Elsaesser HJ, and Brooks DG (2016). Overcoming CD4 Th1 Cell Fate Restrictions to Sustain Antiviral CD8 T Cells and Control Persistent Virus Infection. Cell Rep. 16, 3286–3296. [PubMed: 27653690]
13. Aubert RD, Kamphorst AO, Sarkar S, Vezys V, Ha S-J, Barber DL, Ye L, Sharpe AH, Freeman GJ, and Ahmed R (2011). Antigen-specific CD4 T-cell help rescues exhausted CD8 T cells during chronic viral infection. Proc. Natl. Acad. Sci. USA 108, 21182–21187. [PubMed: 22160724]

14. Vigano S, Bobisse S, Coukos G, Perreau M, and Harari A (2020). Cancer and HIV-1 Infection: Patterns of Chronic Antigen Exposure. Front. Immunol. 11, 1350. [PubMed: 32714330]
15. Han A, Glanville J, Hansmann L, and Davis MM (2014). Linking T-cell receptor sequence to functional phenotype at the single-cell level. Nat. Biotechnol. 32, 684–692. 10.1038/nbt.2938. [PubMed: 24952902]
16. Zhang L, Yu X, Zheng L, Zhang Y, Li Y, Fang Q, Gao R, Kang B, Zhang Q, Huang JY, et al. (2018). Lineage tracking reveals dynamic relationships of T cells in colorectal cancer. Nature 564, 268–272. [PubMed: 30479382]
17. Xydia M, Rahbari R, Ruggiero E, Macaulay I, Tarabichi M, Loh-mayer R, Wilkening S, Michels T, Brown D, Vanuytven S, et al. (2021). Common clonal origin of conventional T cells and induced regulatory T cells in breast cancer patients. Nat. Commun. 12, 1119. [PubMed: 33602930]
18. van Lier RA, Borst J, Vroom TM, Klein H, Van Mourik P, Zeijle-maker WP, and Melief CJ (1987). Tissue distribution and biochemical and functional properties of Tp55 (CD27), a novel T cell differentiation antigen. J. Immunol. 139, 1589–1596. [PubMed: 2442250]
19. Weber LM, Nowicka M, Soneson C, and Robinson MD (2019). diffcyt: Differential discovery in high-dimensional cytometry via high-resolution clustering. Commun. Biol. 2, 183. [PubMed: 31098416]
20. Cachot A, Bilous M, Liu YC, Li X, Saillard M, Cenerenti M, Rockinger GA, Wyss T, Guillaume P, Schmidt J, et al. (2021). Tumor-specific cytolytic CD4 T cells mediate immunity against human cancer. Sci. Adv. 7, eabe3348. 10.1126/sciadv.abe3348. [PubMed: 33637530]
21. Ghorani E, Reading JL, Henry JY, Massy M.R.d., Rosenthal R, Turati V, Joshi K, Furness AJS, Ben Aissa A, Saini SK, et al. (2020). The T cell differentiation landscape is shaped by tumour mutations in lung cancer. Nat. Can. (Ott.) 1, 546–561.
22. Veatch JR, Lee SM, Shasha C, Singhi N, Szeto JL, Moshiri AS, Kim TS, Smythe K, Kong P, Fitzgibbon M, et al. (2022). Neoantigen-specific CD4(+) T cells in human melanoma have diverse differentiation states and correlate with CD8(+) T cell, macrophage, and B cell function. Cancer Cell 40, 393–409.e9. [PubMed: 35413271]
23. Cimmino L, Martins GA, Liao J, Magnusdottir E, Grunig G, Perez RK, and Calame KL (2008). Blimp-1 attenuates Th1 differentiation by repression of ifng, tbx21, and bcl6 gene expression. J. Immunol. 181, 2338–2347. [PubMed: 18684923]
24. Pearce EL (2010). Metabolism in T cell activation and differentiation. Curr. Opin. Immunol. 22, 314–320. [PubMed: 20189791]
25. Kouidhi S, Elgaaied AB, and Chouaib S (2017). Impact of Metabolism on T-Cell Differentiation and Function and Cross Talk with Tumor Microenvironment. Front. Immunol. 8, 270. [PubMed: 28348562]
26. Hartmann FJ, Mrdjen D, McCaffrey E, Glass DR, Greenwald NF, Bharadwaj A, Khair Z, Verberk SGS, Baranski A, Baskar R, et al. (2021). Single-cell metabolic profiling of human cytotoxic T cells. Nat. Biotechnol. 39, 186–197. [PubMed: 32868913]
27. Johnston RJ, Poholek AC, DiToro D, Yusuf I, Eto D, Barnett B, Dent AL, Craft J, and Crotty S (2009). Bcl6 and Blimp-1 are reciprocal and antagonistic regulators of T follicular helper cell differentiation. Science 325, 1006–1010. [PubMed: 19608860]
28. Chang CH, Curtis JD, Maggi LB Jr., Faubert B, Villarino AV, O'Sullivan D, Huang SCC, van der Windt GJW, Blagih J, Qiu J, et al. (2013). Posttranscriptional control of T cell effector function by aerobic glycolysis. Cell 153, 1239–1251. [PubMed: 23746840]
29. Minchenko O, Opentanova I, Minchenko D, Ogura T, and Esumi H (2004). Hypoxia induces transcription of 6-phosphofructo-2-kinase/fructose-2,6-biphosphatase-4 gene via hypoxia-inducible factor-1alpha activation. FEBS Lett. 576, 14–20. [PubMed: 15474002]
30. Zhang H, Zheng Y, Gao H, Xu P, Wang M, Li A, Miao M, Xie X, Deng Y, Zhou H, and Du H (2016). HIF-1a activates hypoxia-induced PFKFB4 expression in human bladder cancer cells. Biochem. Biophys. Res. Commun. 6, 146–152.
31. Johnson MO, Wolf MM, Madden MZ, Andrejeva G, Sugiura A, Contreras DC, Maseda D, Liberti MV, Paz K, Kishton RJ, et al. (2018). Distinct Regulation of Th17 and Th1 Cell Differentiation by Glutaminase-Dependent Metabolism. Cell 175, 1780–1795.e19. [PubMed: 30392958]

32. Ahmadian M, Suh JM, Hah N, Liddle C, Atkins AR, Downes M, and Evans RM (2013). PPARg signaling and metabolism: the good, the bad and the future. Nat. Med. 19, 557–566. [PubMed: 23652116]
33. Hernandez-Quiles M, Broekema MF, and Kalkhoven E (2021). PPAR-gamma in Metabolism, Immunity, and Cancer: Unified and Diverse Mechanisms of Action. Front. Endocrinol. 12, 624112.
34. Ye G, Gao H, Wang Z, Lin Y, Liao X, Zhang H, Chi Y, Zhu H, and Dong S (2019). PPARα and PPARγ activation attenuates total free fatty acid and triglyceride accumulation in macrophages via the inhibition of Fatp1 expression. Cell Death Dis. 10, 39. [PubMed: 30674874]
35. Chinetti G, Lestavel S, Bocher V, Remaley AT, Neve B, Torra IP, Teissier E, Minnich A, Jaye M, Duverger N, et al. (2001). PPAR-alpha and PPAR-gamma activators induce cholesterol removal from human macrophage foam cells through stimulation of the ABCA1 pathway. Nat. Med. 7, 53–58. [PubMed: 11135616]
36. Widenmaier SB, Snyder NA, Nguyen TB, Arduini A, Lee GY, Arruda AP, Saksi J, Bartelt A, and Hotamisligil GS (2017). NRF1 Is an ER Membrane Sensor that Is Central to Cholesterol Homeostasis. Cell 171, 1094–1109.e15. 10.1016/j.cell.2017.10.003. [PubMed: 29149604]
37. Jain J, McCaffrey PG, Valge-Archer VE, and Rao A (1992). Nuclear factor of activated T cells contains Fos and Jun. Nature 356, 801–804. [PubMed: 1533441]
38. Martinez RJ, Zhang N, Thomas SR, Nandiwada SL, Jenkins MK, Binstadt BA, and Mueller DL (2012). Arthritogenic self-reactive CD4+ T cells acquire an FR4hiCD73hi anergic state in the presence of Foxp3+ regulatory T cells. J. Immunol. 188, 170–181. [PubMed: 22124124]
39. García-Bernal D, Dios-Esponera A, Sotillo-Mallo E, García-Verdugoı R, Arellano-Sánchez N, and Teixidó J (2011). RGS10 restricts upregulation by chemokines of T cell adhesion mediated by α4b1 and αLb2 integrins. J. Immunol. 187, 1264–1272. [PubMed: 21705617]
40. Jiang Y, Gao Q, Wang LY, Ma T, Zhu FL, Wang Q, Gao F, Guo C, and Zhang LN (2019). Deficiency of programmed cell death 4 affects the balance of T cell subsets in hyperlipidemic mice. Mol. Immunol. 112, 387–393. [PubMed: 31288148]
41. Lingel H, Wissing J, Arra A, Schanze D, Lienenklaus S, Klawonn F, Pierau M, Zenker M, Jänsch L, and Brunner-Weinzierl MC (2017). CTLA-4-mediated posttranslational modifications direct cytotoxic T-lymphocyte differentiation. Cell Death Differ. 24, 1739–1749. [PubMed: 28644433]
42. Corapi E, Carrizo G, Compagno D, and Laderach D (2018). Endogenous Galectin-1 in T Lymphocytes Regulates Anti-prostate Cancer Immunity. Front. Immunol. 9, 2190. [PubMed: 30319642]
43. Cedeno-Laurent F, Watanabe R, Teague JE, Kupper TS, Clark RA, and Dimitroff CJ (2012). Galectin-1 inhibits the viability, proliferation, and Th1 cytokine production of nonmalignant T cells in patients with leukemic cutaneous T-cell lymphoma. Blood 119, 3534–3538. [PubMed: 22383798]
44. Javanmard Khameneh H, Leong KWK, Mencarelli A, Vacca M, Mambwe B, Neo K, Tay A, Zolezzi F, Lee B, and Mortellaro A (2019). The Inflammasome Adaptor ASC Intrinsically Limits CD4+ T-Cell Proliferation to Help Maintain Intestinal Homeostasis. Front. Immunol. 10, 1566. [PubMed: 31379813]
45. Sebzda E, Zou Z, Lee JS, Wang T, and Kahn ML (2008). Transcription factor KLF2 regulates the migration of naive T cells by restricting chemokine receptor expression patterns. Nat. Immunol. 9, 292–300. [PubMed: 18246069]
46. Weinreich MA, Takada K, Skon C, Reiner SL, Jameson SC, and Hogquist KA (2009). KLF2 transcription-factor deficiency in T cells results in unrestrained cytokine production and upregulation of bystander chemokine receptors. Immunity 31, 122–130. [PubMed: 19592277]
47. Cao J, Spielmann M, Qiu X, Huang X, Ibrahim DM, Hill AJ, Zhang F, Mundlos S, Christiansen L, Steemers FJ, et al. (2019). The single-cell transcriptional landscape of mammalian organogenesis. Nature 566, 496–502. [PubMed: 30787437]
48. Trapnell C, Cacchiarelli D, Grimsby J, Pokharel P, Li S, Morse M, Lennon NJ, Livak KJ, Mikkelsen TS, and Rinn JL (2014). The dynamics and regulators of cell fate decisions are revealed by pseudotemporal ordering of single cells. Nat. Biotechnol. 32, 381–386. [PubMed: 24658644]

49. Qiu X, Mao Q, Tang Y, Wang L, Chawla R, Pliner HA, and Trapnell C (2017). Reversed graph embedding resolves complex single-cell trajectories. Nat. Methods 14, 979–982. [PubMed: 28825705]
50. Chi H (2012). Regulation and function of mTOR signalling in T cell fate decisions. Nat. Rev. Immunol. 12, 325–338. [PubMed: 22517423]
51. Chen Z, Ji Z, Ngiow SF, Manne S, Cai Z, Huang AC, Johnson J, Staupe RP, Bengsch B, Xu C, et al. (2019). TCF-1-Centered Transcriptional Network Drives an Effector versus Exhausted CD8 T Cell-Fate Decision. Immunity 51, 840–855.e5. [PubMed: 31606264]
52. Khatun A, Kasmani MY, Zander R, Schauder DM, Snook JP, Shen J, Wu X, Burns R, Chen YG, Lin CW, et al. (2021). Single-cell lineage mapping of a diverse virus-specific naive CD4 T cell repertoire. J. Exp. Med. 218, e20200650. [PubMed: 33201171]
53. Zander R, Khatun A, Kasmani MY, Chen Y, and Cui W (2022). Delineating the transcriptional landscape and clonal diversity of virus-specific CD4+ T cells during chronic viral infection. Elife 11, e80079. [PubMed: 36255051]
54. Xu K, Wang R, Xie H, Hu L, Wang C, Xu J, Zhu C, Liu Y, Gao F, Li X, et al. (2021). Single-cell RNA sequencing reveals cell heterogeneity and transcriptome profile of breast cancer lymph node metastasis. Oncogenesis 10, 66. [PubMed: 34611125]
55. Kim N, Kim HK, Lee K, Hong Y, Cho JH, Choi JW, Lee J-I, Suh Y-L, Ku BM, Eum HH, et al. (2020). Single-cell RNA sequencing demonstrates the molecular and cellular reprogramming of metastatic lung adenocarcinoma. Nat. Commun. 11, 2285. [PubMed: 32385277]
56. Ng SS, De Labastida Rivera F, Yan J, Corvino D, Das I, Zhang P, Kuns R, Chauhan SB, Hou J, Li X-Y, et al. (2020). The NK cell granule protein NKG7 regulates cytotoxic granule exocytosis and inflammation. Nat. Immunol. 21, 1205–1218. [PubMed: 32839608]
57. Bruniquel D, Borie N, Hannier S, and Triebel F (1998). Regulation of expression of the human lymphocyte activation gene-3 (LAG-3) molecule, a ligand for MHC class II. Immunogenetics 48, 116–124. [PubMed: 9634475]
58. Annunziato F, Manetti R, Cosmi L, Galli G, Heusser CH, Romagnani S, and Maggi E (1997). Opposite role for interleukin-4 and interferon-gamma on CD30 and lymphocyte activation gene-3 (LAG-3) expression by activated naive T cells. Eur. J. Immunol. 27, 2239–2244. [PubMed: 9341765]
59. McLane LM, Ngiow SF, Chen Z, Attanasio J, Manne S, Ruthel G, Wu JE, Staupe RP, Xu W, Amaravadi RK, et al. (2021). Role of nuclear localization in the regulation and function of T-bet and Eomes in exhausted CD8 T cells. Cell Rep. 35, 109120. [PubMed: 33979613]
60. Yost KE, Satpathy AT, Wells DK, Qi Y, Wang C, Kageyama R, McNamara KL, Granja JM, Sarin KY, Brown RA, et al. (2019). Clonal replacement of tumor-specific T cells following PD-1 blockade. Nat. Med. 25, 1251–1259. [PubMed: 31359002]
61. Klein Geltink RI, O'Sullivan D, Corrado M, Bremser A, Buck MD, Buescher JM, Firat E, Zhu X, Niedermann G, Caputa G, et al. (2017). Mitochondrial Priming by CD28. Cell 171, 385–397.e11. [PubMed: 28919076]
62. Reina-Campos M, Scharping NE, and Goldrath AW (2021). CD8+ T cell metabolism in infection and cancer. Nat. Rev. Immunol. 21, 718–738. [PubMed: 33981085]
63. Møller SH, Hsueh P-C, Yu Y-R, Zhang L, and Ho P-C (2022). Metabolic programs tailor T cell immunity in viral infection, cancer, and aging. Cell Metabol. 34, 378–395.
64. Mailer RKW, Gisterå A, Polyzos KA, Ketelhuth DFJ, and Hansson GK (2017). Hypercholesterolemia Enhances T Cell Receptor Signaling and Increases the Regulatory T Cell Population. Sci. Rep. 7, 15655. [PubMed: 29142309]
65. McInnes L, Healy J, and Melville J (2018). UMAP: Uniform Manifold Approximation and Projection for Dimension Reduction. ArXiv 1802, 03426.
66. Levine JH, Simonds EF, Bendall SC, Davis KL, Amir E.a.D., Tadmor MD, Litvin O, Fienberg HG, Jager A, Zunder ER, et al. (2015). Data-Driven Phenotypic Dissection of AML Reveals Progenitorlike Cells that Correlate with Prognosis. Cell 162, 184–197. [PubMed: 26095251]
67. Hao Y, Hao S, Andersen-Nissen E, Mauck WM, Zheng S, Butler A, Lee MJ, Wilk AJ, Darby C, Zager M, et al. (2021). Integrated analysis of multimodal single-cell data. Cell 184, 3573–3587.e29. [PubMed: 34062119]

68. Brooks DG, McGavern DB, and Oldstone MBA (2006). Reprogramming of antiviral T cells prevents inactivation and restores T cell activity during persistent viral infection. J. Clin. Invest. 116, 1675–1685. [PubMed: 16710479]
69. Gett AV, and Hodgkin PD (2000). A cellular calculus for signal integration by T cells. Nat. Immunol. 1, 239–244. [PubMed: 10973282]
70. Wu Y, Borde M, Heissmeyer V, Feuerer M, Lapan AD, Stroud JC, Bates DL, Guo L, Han A, Ziegler SF, et al. (2006). FOXP3 controls regulatory T cell function through cooperation with NFAT. Cell 126, 375–387. [PubMed: 16873067]
71. Naviaux RK, Costanzi E, Haas M, and Verma IM (1996). The pCL vector system: rapid production of helper-free, high-titer, recombinant retroviruses. J. Virol. 70, 5701–5705. [PubMed: 8764092]
72. Kowarz E, Löscher D, and Marschalek R (2015). Optimized Sleeping Beauty transposons rapidly generate stable transgenic cell lines. Biotechnol. J. 10, 647–653. [PubMed: 25650551]
73. Mátés L, Chuah MKL, Belay E, Jerchow B, Manoj N, Acosta-Sanchez A, Grzela DP, Schmitt A, Becker K, Matrai J, et al. (2009). Molecular evolution of a novel hyperactive Sleeping Beauty transposase enables robust stable gene transfer in vertebrates. Nat. Genet. 41, 753–761. [PubMed: 19412179]
74. Xu W, Snell LM, Guo M, Boukhaled G, Macleod BL, Li M, Tullius MV, Guidos CJ, Tsao MS, Divangahi M, et al. (2021). Early innate and adaptive immune perturbations determine long-term severity of chronic virus and Mycobacterium tuberculosis coinfection. Immunity 54, 526–541.e7. [PubMed: 33515487]
75. Subramanian A, Tamayo P, Mootha VK, Mukherjee S, Ebert BL, Gillette MA, Paulovich A, Pomeroy SL, Golub TR, Lander ES, and Mesirov JP (2005). Gene set enrichment analysis: A knowledge-based approach for interpreting genome-wide expression profiles. Proc. Natl. Acad. Sci. USA 102, 15545–15550. [PubMed: 16199517]
76. Mootha VK, Lindgren CM, Eriksson K-F, Subramanian A, Sihag S, Lehar J, Puigserver P, Carlsson E, Ridderstråle M, Laurila E, et al. (2003). PGC-1α-responsive genes involved in oxidative phosphorylation are coordinately downregulated in human diabetes. Nat. Genet. 34, 267–273. [PubMed: 12808457]
77. Wei G, Wei L, Zhu J, Zang C, Hu-Li J, Yao Z, Cui K, Kanno Y, Roh TY, Watford WT, et al. (2009). Global mapping of H3K4me3 and H3K27me3 reveals specificity and plasticity in lineage fate determination of differentiating CD4+ T cells. Immunity 30, 155–167. [PubMed: 19144320]
78. Haribhai D, Lin W, Edwards B, Ziegelbauer J, Salzman NH, Carlson MR, Li SH, Simpson PM, Chatila TA, and Williams CB (2009). A central role for induced regulatory T cells in tolerance induction in experimental colitis. J. Immunol. 182, 3461–3468. [PubMed: 19265124]

## Highlights

- CD4 $T_{TS}$ cells are primed but rapidly “paralyzed” in the dLN during tumor development
- Tregs and CTLA4 halt CD4 $T_{TS}$ cell activation, freezing proliferation, and differentiation
- CD4 $T_{TS}$ cells retain latent functional capacity to resume tumor infiltration
- Overcoming CD4 $T_{TS}$ cells paralysis enhances long-term tumor control

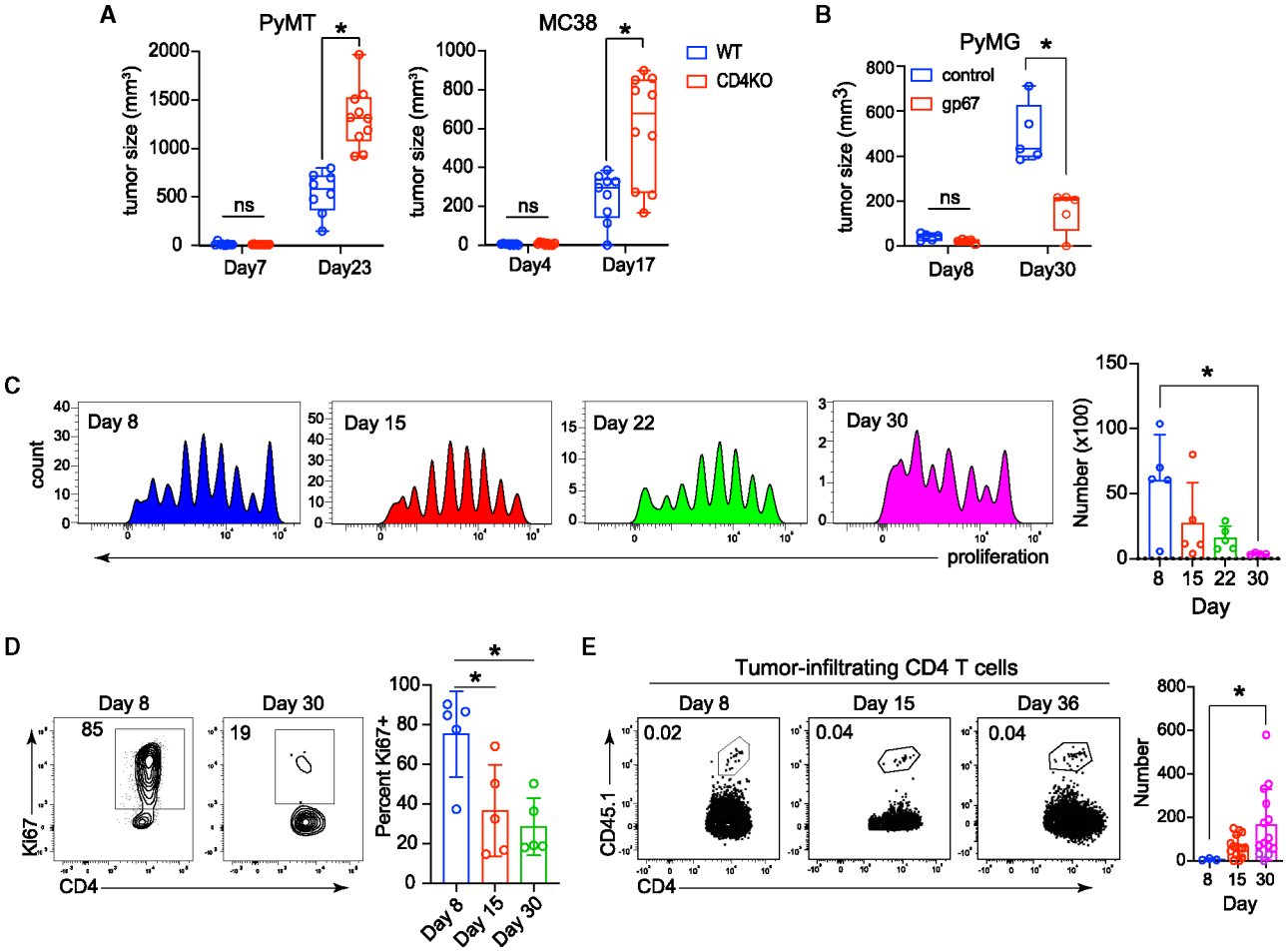


**Figure 1. Sub-optimal help and rapidly blunted proliferation of CD4 $T_{TS}$ cells**

(A) Tumor sizes of PyMT and MC38 tumor cells in WT and CD4 knockout (KO) mice at the indicated time points.

(B) Mice received naive CD4 SMARTA $T_{TS}$ cells followed by implantation of PyMG tumors. On the same day of tumor implantation, mice received unlabeled or $GP_{61–80}$ peptide-labeled β2m−/− bmDC. Bar graph shows the tumor size at the indicated day.

(C–E) TAGIT proliferation dye-labeled naive SMARTA cells were transferred into WT mice followed by PyMG injection. (C) Histograms show TAGIT dilution on the indicated day. The bar graph represents the total number of CD4 SMARTA $T_{TS}$ cells in the dLN at the indicated day after PyMG administration. (D) Expression (flow plot) and the percentage of Ki67+ out of total CD4 SMARTA $T_{TS}$ cells (gated on SMARTA cells) in the dLN. (E) Representative percentage (flow plots) and number (bar graph) of CD4 SMARTA $T_{TS}$ cells in the tumor at each time point. Data represent three independent experiments with at least five mice per group. Error bars indicate standard deviation (SD). For comparison of tumor growth kinetics, significance is determined by two-way ANOVA; for other comparisons, significance is determined by Mann-Whitney U test. *p < 0.05.

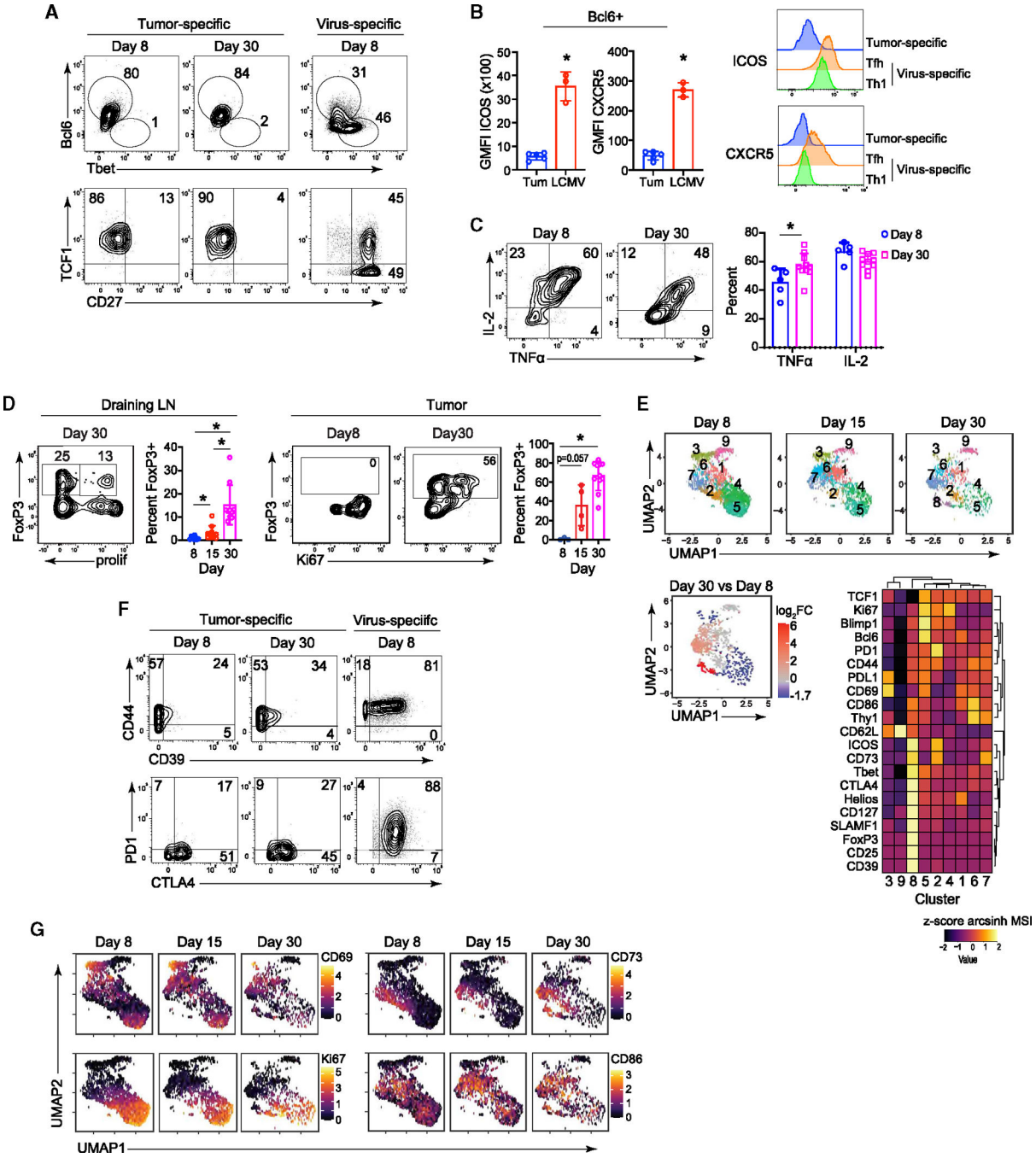


**Figure 2. Incomplete differentiation and selective function of CD4 $T_{TS}$ cells**

(A) Representative expression of the indicated protein CD4 SMARTA $T_{TS}$ cells (in the dLN) on the indicated day. Virus-specific CD4 SMARTA T cells from chronic LCMV infection are shown for comparison.

(B) Geometric mean fluorescence intensity (GMFI) of ICOS and CXCR5 by Bcl6+ tumor-specific or virus-specific CD4 SMARTA Tfh cells (bar graphs). Histograms show representative ICOS and CXCR5 expression by dLN tumor-specific SMARTA cells, and by virus-specific CD4 Th1 and Tfh cells.

(C) Expression and quantification of TNF-α- and IL-2-producing CD4 SMARTA T cells in dLN after *ex vivo* LCMV-$GP_{61–80}$ peptide stimulation.
(D) (Left) FoxP3 versus TAGIT expression by CD4 SMARTA $T_{TS}$ cells on day 30 in the dLN. The bar graph is gated on CD4 SMARTA $T_{TS}$ cells and shows the percentage of FoxP3+ cells in the dLN. (Right) Plots show the cycling (Ki67+) FoxP3+ CD4 SMARTA $T_{TS}$ cells in the PyMG tumor. The bar graphs show the percentage of FoxP3+ SMARTA $T_{TS}$ cells in the tumor.
(E) (Top) UMAP embeddings of CyTOF data of CD4 SMARTA $T_{TS}$ cells in the dLN at days 8, 15, and 30 after PyMG initiation. Cells are colored by Phenograph clustering. Data are concatenated from five to seven mice per group. (Bottom) UMAP plot shows the clusters that are increased (red) or decreased (blue) in abundance from day 8 to 30. The bar graph indicates the log2 fold change of each cluster and the associated significance (calculated using diffcyt,[19] *adjusted p value < 0.05). Heatmap depicts the normalized Z scores of the arcsinh-transformed median signal intensity (MSI) of the indicated protein in each cluster.
(F) Expression of the indicated proteins by CD4 SMARTA $T_{TS}$ cells in the dLN. Virus-specific CD4 SMARTA T cells from chronic LCMV infection are shown for comparison.
(G) UMAPs show the arcsinh-transformed single-cell expression of the indicated proteins by CD4 SMARTA $T_{TS}$ cells in the dLN at each time point. For flow cytometry, data represent three independent experiments with at least five mice per group. Error bars indicate SD. Significance is determined by Mann-Whitney U test. *p < 0.05. CyTOF data are representative of two experiments with at least three mice per group.

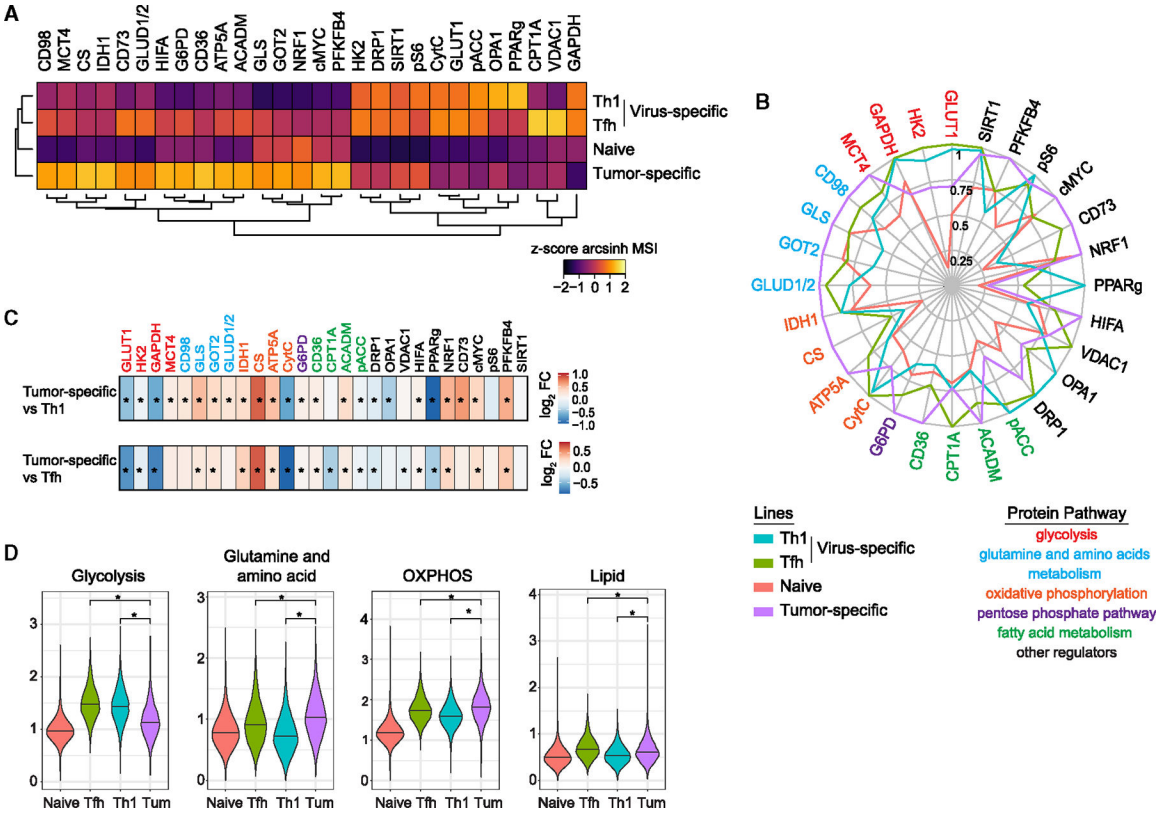


**Figure 3. CyTOF analyses of CD4 $T_{TS}$ cell metabolic pathways.**

CD4 SMARTA T cells were transferred into WT mice followed by PyMG tumor injection or acute LCMV-Armstrong infection. On day 8, SMARTA cells from tumor dLN or spleen of LCMV-infected mice were isolated. SMARTA cells from uninfected mice were used as naive control.

(A) Heatmap depicts the normalized *Z* scores of the arcsinh-transformed MSI of the indicated protein for each cluster.

(B) Radar plot depicts the relative arcsinh-transformed MSI of the indicated proteins by each group, scaling as the percentage of the highest expression.

(C) Heatmaps show the differential state comparisons (calculated by diffcyt[19]) between tumor-specific CD4 SMARTA T cells and LCMV-specific CD4 Th1 (top) or Tfh (bottom) SMARTA T cells. Coloration shows log2 fold change. *adjusted p value < 0.05.

(D) Violin plots show the single-cell scoring of each metabolic pathway calculated as described in STAR Methods. Statistics were performed Wilcox test only comparing CD4 $T_{TS}$ cells with Th1 and Tfh. *p < 0.05. Data are representative of two experiments with at least three mice per group.

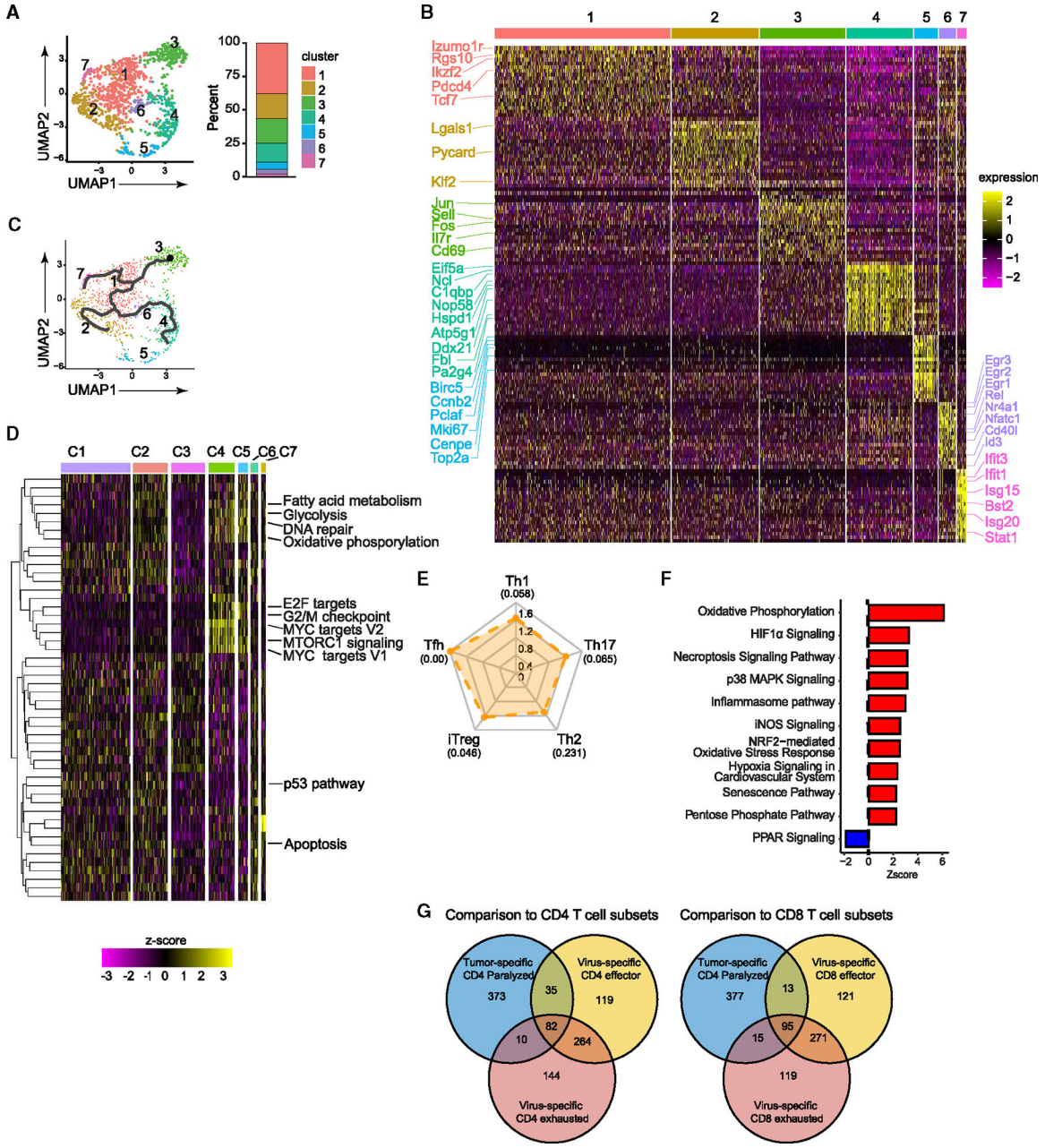


**Figure 4. Transcriptional programming of CD4 T cell paralysis in dLN by scRNA-seq**

(A) Seurat clustering (resolution 0.5) of CD4 $T_{TS}$ cells. The bar graph depicts the proportion of each cluster.

(B) Top 20 differentially expressed genes (DEGs) of each cluster.

(C)Monocle trajectory analysis overlaid on UMAP colored by Seurat clusters. </p/> (D) Single-cell heatmap depicts gene set variation analysis pathway analysis within each Seurat cluster.

(E) Radar plot shows normalized enrichment scores of GSEA comparing CD4 SMARTA $T_{TS}$ cells from c4 (see Figure S4E) with defined Th cell lineage signatures. Numbers in parentheses are the FDR. A value of 0.00 = FDR < $10^{-3}$.

(F) IPA pathway enrichment scoring of CD4 SMARTA $T_{TS}$ cells in c4 (see Figure S4E). All included pathways are significant with $p < 0.05$. Pathways colored in red were specifically mentioned in the text.

(G) Venn diagrams show the overlap and difference in DEGs of paralyzed tumor CD4 $T_{TS}$ cells, effector and exhausted virus-specific CD4 (left) and CD8 T cells (right). Each group was individually compared with naive T cells first prior to the comparisons shown. The numbers indicate the number of genes.

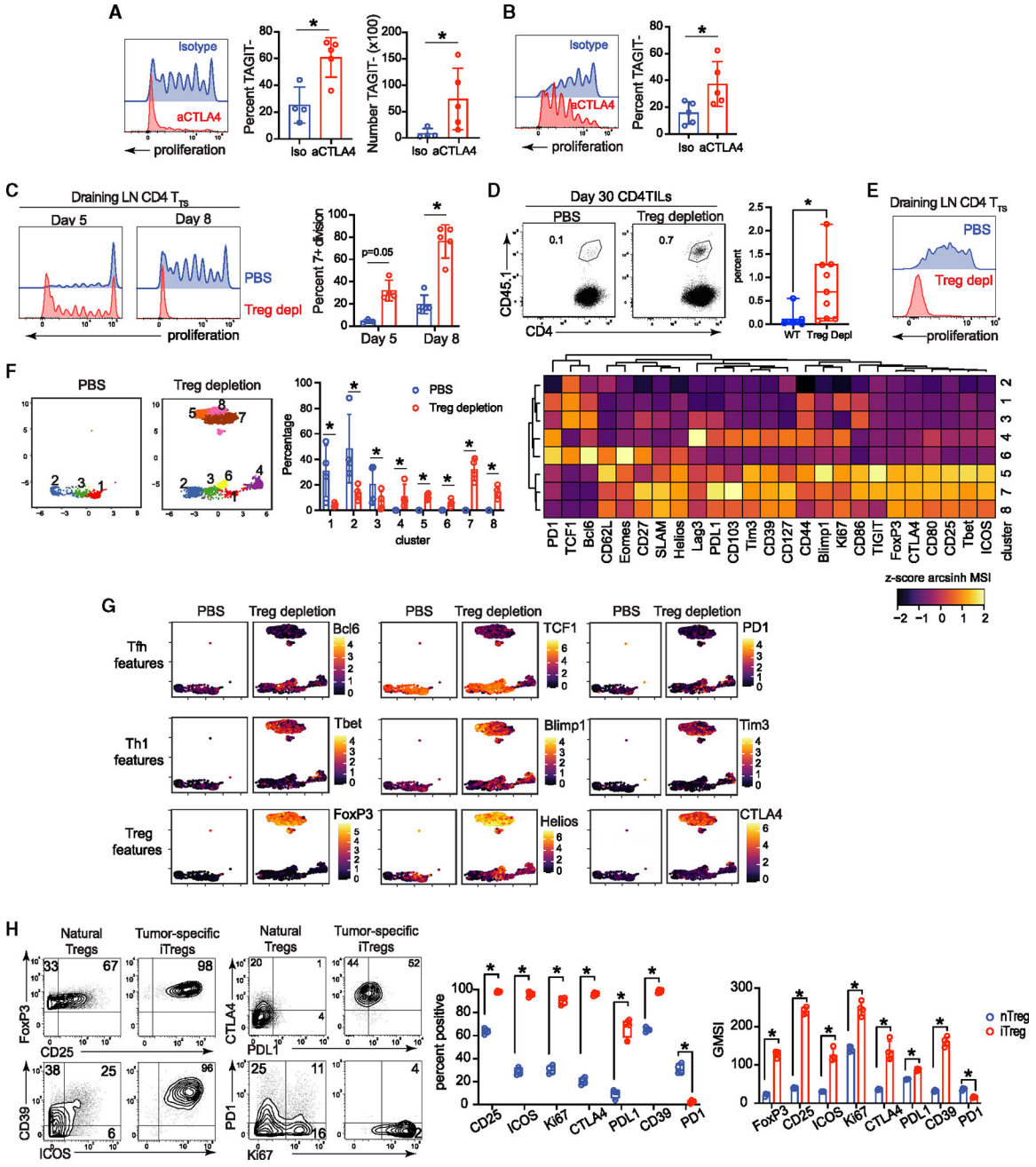


**Figure 5. CTLA4 and Tregs reciprocally induce paralysis of CD4 $T_{TS}$ cells.**

(A and B) On days 0, 2, and 5 (A) or days 21, 23, and 26 (B) after PyMG administration, mice were treated with 300 μg CTLA4 blocking or isotype control antibodies. Histogram shows proliferation of SMARTA cells on (A) day 8 or (B) day 29 in the dLN. Bar graphs show the frequency and number of SMARTA cells that completely diluted TAGIT.

(C–H) FoxP3-DTR mice received TAGIT-labeled naive SMARTA cells followed by PyMG injection and either PBS or diphtheria toxin (DT) treatment. </p/> (C) Histograms show the proliferation of CD4 SMARTA $T_{TS}$ cells in the dLN on the indicated day. The bar graph shows the percentage of CD4 SMARTA $T_{TS}$ cells that have completely diluted TAGIT.

(D) Flow plots and bar graph depict the frequency of SMARTA cells of CD4 T cells in the tumor at day 30.

(E) FoxP3-DTR mice were treated with PBS or DT on days 21 and 23 after PyMG injection. Histograms show the proliferation of CD4 SMARTA $T_{TS}$ cells in the dLN on day 29 (8 days after treatment).

(F) UMAP plots indicating PhenoGraph clusters of CD4 SMARTA $T_{TS}$ cells in dLN 8 days after PyMG initiation (concatenated from four to five mice in each group). Bar graph shows the frequency of each cluster, with each circle representing the percent of SMARTA $T_{TS}$ cells in that cluster from an individual mouse. *adjusted p value < 0.05, calculated by diffcyt. Heatmap depicts the normalized Z scores of the arcsinh-transformed MSI of the indicated protein for each cluster.

(G) UMAPs show the single-cell arcsinh-transformed expression of the indicated protein by CD4 SMARTA $T_{TS}$ cells.

(H) Expression of the indicated protein on SMARTA iTreg (c5, 7, and 8) and Tregs (FoxP3+ Helios+ of non-SMARTA CD4 T cells in dLN, from PBS control-treated mice). Bar graphs show the frequency (left) and GMSI (geometric mean of arcsinh-transformed MSI calculated by FlowJo) (right) of the indicated protein in the Tregs or SMARTA iTregs. Data represent two to three independent experiments with at least four mice per group. Error bars indicate SD. Significance other than CyTOF analyses is determined by Mann-Whitney U test. *p < 0.05.

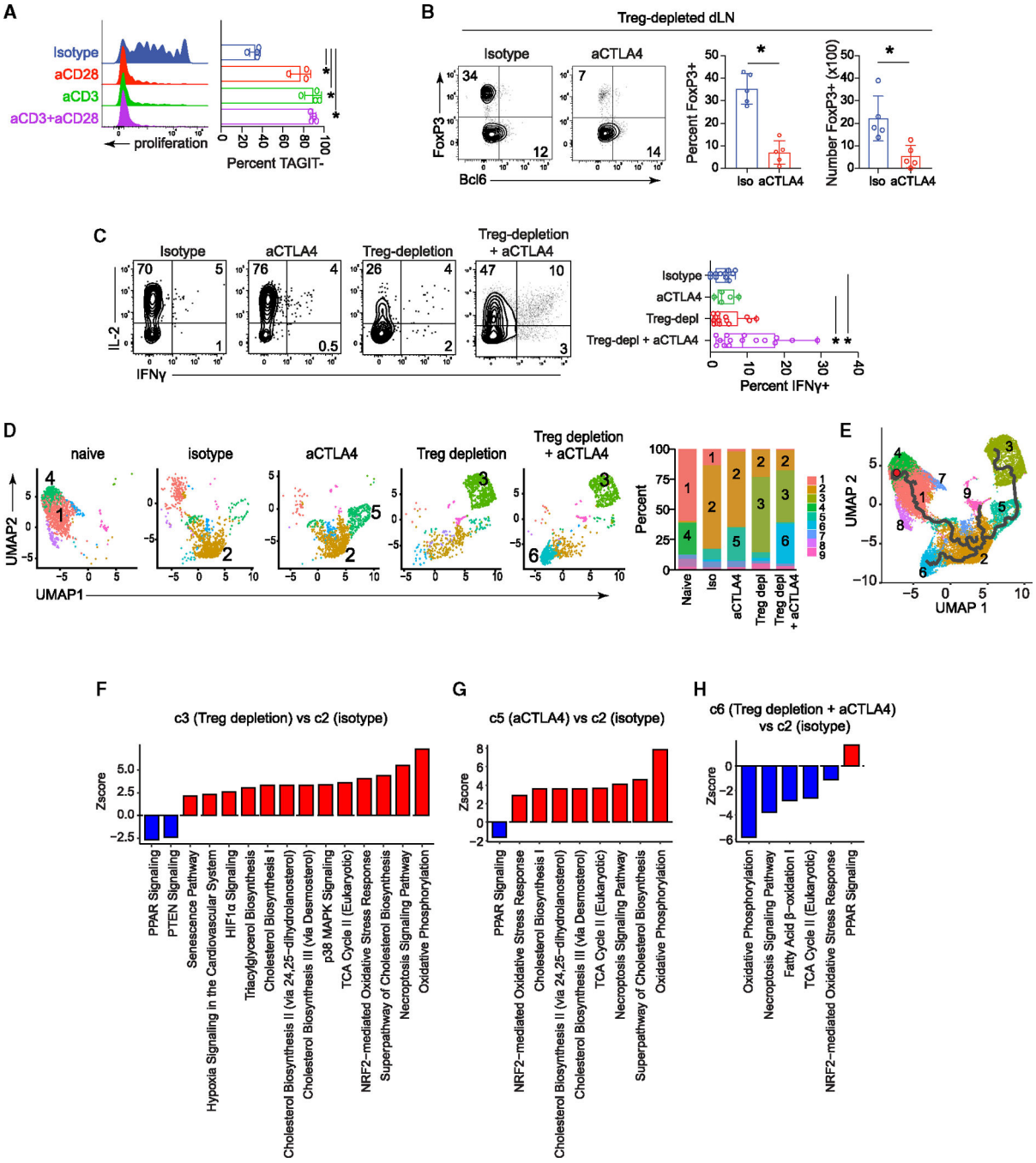


**Figure 6. CTLA4 drives tumor-specific iTreg differentiation in Treg-depleted mice and dual Treg depletion and CTLA4 blockade enable effector differentiation and metabolic re-organization**

(A) On day 5 after PyMG administration, mice received isotype control, anti-CD3 alone, anti-CD28 alone, or dual anti-CD3 and anti-CD28 antibodies. Cell proliferation of CD4 SMARTA $T_{TS}$ cells in dLN was analyzed on day 8.

(B and C) FoxP3-DTR mice were treated on days 0 and 2 with DT, and on days 0, 2, and 5 with CTLA4-blocking or isotype antibodies. </p/> (B) Expression of FoxP3 and Bcl6 by SMARTA cells. Bar graphs show the frequency (left) and number (right) of FoxP3+ SMARTA cells.

(C) Cytokine production by CD4 SMARTA $T_{TS}$ cells after *ex vivo* restimulation.
(D–H) FoxP3-DTR mice were treated on days 0 and 2 with PBS or DT; and/or on days 0, 2, and 5 with CTLA4-blocking or isotype antibodies. Analysis was performed on dLN SMARTA $T_{TS}$ cells on day 8 after PyMG administration.
(D) UMAP plots show Seurat clustering (resolution 0.3) of CD4 SMARTA $T_{TS}$ cells s in each condition. Bar graph depicts the proportion of each cluster. The numbers in the stacked bar graphs indicate the cluster.
(E) Monocle trajectory analysis overlaid onto the Seurat clustered UMAP (all conditions combined).
(F–H) IPA pathways enrichment scoring of the indicated clusters. All pathways are significant with a p value < 0.05. For (A)–(C), the data represent three independent experiments with at least five mice per group. Error bars indicate SD. Significance is determined by Mann-Whitney U test. *p < 0.05.

## KEY RESOURCES TABLE

| REAGENT or RESOURCE | SOURCE | IDENTIFIER |
|---|---|---|
| Antibodies | | |
| Y(89)-*anti*-MHCII (Clone M5/114.15.2) | Biolegend | Cat#107602; RRID: AB_313317 |
| 115In-*anti*-Ly6C (Clone HK14) | Biolegend | Cat#128001; RRID: AB_1134213 |
| 141Pr-*anti*-CD44 (Clone IM7) | Biolegend | Cat#103001; RRID: AB_312952 |
| 116Cd-*anti*-GranzymeB (Clone GB11) | Invitrogen | Cat#MA1-80734; RRID: AB_931084 |
| 142Nd-*anti*-CXCR5 (Clone L138D7) | Biolegend | Cat#145502; RRID: AB_2561955 |
| 143Nd-*anti*-CD45.2 (Clone 104) | Biolegend | Cat#109802; RRID: AB_313439 |
| 116Cd-*anti*-CD45.2 (Clone 104) | Biolegend | Cat#109802; RRID: AB_313439 |
| 145Nd-*anti*-CTLA-4 (Clone UC10-4B9) | Biolegend | Cat#106302; RRID: AB_313251 |
| 146Nd-*anti*-EOMES (Clone Dan11mag) | eBioscience | Cat#14-4875-82; RRID: AB_11042577 |
| 148Nd-*anti*-ICOS (Clone C398.4A) | Fluidigm | Cat#3148019B; RRID: AB_2756435 |
| 149Sm-*anti*-CD69 (Clone H1.273) | Biolegend | Cat#104502; RRID: AB_313105 |
| 150Nd-*anti*-CD73 (Clone TY/11.8) | Biolegend | Cat#127202; RRID: AB_1089066 |
| 151Eu-*anti*-CD25 (Clone 3C7) | Fluidigm | Cat#3151007B; RRID: AB_2827880 |
| 152Sm-*anti*-CD86 (Clone GL-1) | Biolegend | Cat#105007; RRID: AB_313150 |
| 153Eu-*anti*-PDL1(Clone M1H5) | eBioscience | Cat#14-5982-82; RRID: AB_467781 |
| 154Eu-*anti*-CD45.1 (Clone A20) | eBioscience | Cat#14-0453-82; RRID: AB_467258 |
| 155Gd-*anti*-CD103 (Clone M290) | BD Bioscience | Cat#553699; RRID: AB_394995 |
| 156Gd-*anti*-CD27 (Clone LG.3A10) | Biolegend | Cat#124202; RRID: AB_1236456 |
| 158Gd-*anti*-RORɣt (Clone Q31-378) | BD Biosciences | Cat#562197; RRID: AB_10894594 |
| 159Tb-*anti*-CD39 (Clone 24DMS1) | eBioscience | Cat#14-0391-82; RRID: AB_1210501 |
| 142Nd-*anti*-CD39 (Clone 24DMS1) | eBioscience | Cat#14-0391-82; RRID: AB_1210501 |
| 160Gd-*anti*-CD4 (Clone rm4-5) | Biolegend | Cat#100505; RRID: AB_312708 |
| 161Dy-*anti*-T-bet (Clone 4B10) | Fluidigm | Cat#3161014B; RRID: AB_2858233 |
| 162Dy-*anti*-Foxp3 (Clone MF-14) | Biolegend | Cat#126401; RRID: AB_1089120 |
| 163Dy-*anti*-Foxp3 (Clone MF-14) | Biolegend | Cat#126401; RRID: AB_1089120 |
| 163Dy-*anti*-Tim-3 (Clone B8.2C12) | Biolegend | Cat#134002; RRID: AB_1626128 |
| 164Dy-*anti*-CD62L (Clone MEL-14) | Fluidigm | Cat#3164003B; RRID: AB_2885021 |
| 165Ho-*anti*-TCRb (Clone H57-597) | Biolegend | Cat#109201; RRID: AB_313424 |
| 166Er-*anti*-Blimp1 (Clone ROS195G) | Biolegend | Cat# 648202; RRID:AB_2300132 |
| 167Er-*anti*-TCF-1 (Clone S33-966) | BD Biosciences | Cat#624084; RRID: NA |
| 168Er-*anti*-Bcl6 (Clone K112.91) | BD Biosciences | Cat#561520; RRID: AB_10713172 |
| 169Tm-*anti*-SLAM (Clone TC15-12F12.2) | Biolegend | Cat#115901; RRID: AB_313680 |
| 171Yb-*anti*-CD80 (Clone 16-10A1) | Fluidigm | Cat#3171008B; RRID: AB_2885024 |
| 172Yb-*anti*-Ki67 (Clone B56) | BD Biosciences | Cat#550609; RRID: AB_393778 |
| 173Yb-*anti*-Helios (Clone 22F6) | Biolegend | Cat#137202; RRID: AB_10900638 |
| 174Yb-*anti*-CD127 (Clone A7R34) | Biolegend | Cat#135002; RRID: AB_1937287 |
| 175Lu-*anti*-PD1 (Clone RMP-30) | Biolegend | Cat#109101; RRID: AB_313418 |
| 159Tb-*anti*-PD1 (Clone RMP-30) | Biolegend | Cat#109101; RRID: AB_313418 |

| REAGENT or RESOURCE | SOURCE | IDENTIFIER |
|---|---|---|
| 176Yb-*anti*-Thy1.2 (Clone 53-21) | ThermoFisher | Cat#14-0902-82; RRID: AB_467379 |
| 209Bi*anti*-Lag3 (Clone C9B7W) | Biolegend | Cat#125202; RRID: AB_961187 |
| 174Yb-*anti*-Lag3 (Clone C9B7W) | Biolegend | Cat#125202; RRID: AB_961187 |
| 111Cd-*anti*-PPARg (Clone: polyclonal) | Thermo Fisher | Cat#PA5-25757; RRID: AB_2543257 |
| 112Cd-*anti*-NRF1 (Clone: EPR5554(N)) | Abcam | Cat#ab221792 |
| 114Cd-*anti*-pACC (Clone:D7D11) | Cell signaling | Cat#11818S; RRID: AB_2687505 |
| 141Pr-*anti*-cMYC (Clone Y69) | Abcam | Cat#ab168727 |
| 143Nd-*anti*-GOT2 (clone: poly clonal) | Thermo Fisher | Cat#PA5-35374; RRID: AB_2552684 |
| 144Nd-*anti*-FITC (Clone FIT-22) | Fluidigm | Cat# 3144006B |
| 145Nd-*anti*-MCT4(Clone D-1) | Santa Cruz | Cat#sc-376140; RRID: AB_10992036 |
| 147Sm-*anti*-GAPDH (Clone 6C5) | Thermo Fisher | Cat#AM4300; RRID: AB_2536381 |
| 149Sm-*anti*-CytC (Clone 6H2.B4) | Biolegend | Cat# 612302; RRID: AB_315775 |
| 151Eu-*anti*-ACADM(Clone3B7BH7) | Abcam | Cat# ab110296 |
| 152Sm-*anti*-GLS (Clone polyclonal) | Thermo Fisher | Cat# PA5-35365; RRID: AB_2552675 |
| 153Eu-*anti*-CS(Clone EPR8067) | Abcam | Cat# ab233838 |
| 155Gd-*anti*-HIF1A (Clone 16H4L13) | Thermo Fisher | Cat#700505; RRID: AB_2532327 |
| 156Gd-*anti*-PFKFB4 (Clone polyclonal) | Thermo Fisher | Cat# PA5-15475; RRID: AB_2162868 |
| 158Gd-*anti*-ATP5A (Clone 15H4C4) | Abcam | Cat# ab14748 |
| 161Dy-*anti*-VDAC1(Clone 20B12AF2) | Abcam | Cat# ab14734 |
| 162Dy-*anti*-G6PD (Clone EPR20668) | Abcam | Cat#ab231828 |
| 166Er-*anti*-GLUT1(Clone EPR3915) | Abcam | Cat#ab196357 |
| 169Tm-*anti*-LDHA (Clone EP1566Y) | Abcam | Cat#ab219591 |
| 170Er-*anti*-IDH1 (Clone EPR21002) | Abcam | Cat#ab242078 |
| 171Yb-*anti*-HK2 (Clone EPR20839) | Abcam | Cat#ab228819 |
| 173Yb-*anti*-CPT1A (Clone 8F6AE9) | Abcam | Cat#ab128568 |
| 175Lu-*anti*-GLUD1/2 (Clone D9F7P) | Cell signaling | Cat#12793; RRID: AB_2750880 |
| 176Yb-*anti*-APC(Clone APC003) | Fluidigm | Cat# 3176007B; RRID: AB_2811236 |
| 194Pt-*anti*-OPA1(Clone EPR11057(B)) | abcam | Cat#ab240143 |
| 195Pt-*anti*-DRP1(Clone EPR19274) | abcam | Cat#ab219596 |
| 196Pt-*anti*-pS6(Clone A17020B) | Biolegend | Cat# 608602; RRID: AB_2749899 |
| 198Pt-*anti*-SIRT1 (Clone E104) | abcam | Cat#ab220807 |
| FITC anti-mouse Ki67 (clone 35/Ki-67RUO) | BD Bioscience | Cat#556026; RRID:AB_396302 |
| APCcy7 anti-mouse CD4 (Clone Gk1.5) | Biolegend | Cat# 100414; RRID:AB_312699 |
| BV785 anti-mouse CD4 (Clone Gk1.5) | Biolegend | Cat# 100453; RRID: AB_2565843 |
| PerCP/Cyanine5.5 anti-mouse CD45.1 (clone A20) | Biolegend | Cat#110728; RRID:AB_893346 |
| PE anti-mouse Bcl6 (clone K112-91) | BD Bioscience | Cat#561522; RRID:AB_10717126 |
| APC anti-mouse Tbet (clone 4B10) | Biolegend | Cat#644814; RRID:AB_10901173 |
| FITC anti-mouse ICOS (Clone C398.4A) | Biolegend | Cat#313506; RRID: AB_416330 |
| APC anti-mouse CXCR5(Clone L138D7) | Biolegend | Cat#145506; RRID: AB_2561970 |
| PE anti-mouse SLAMF1/CD150 (Clone TC15-12F12.2) | Biolegend | Cat#115904; RRID: AB_313683 |
| PEcy7 anti-mouse FoxP3 (Clone FJK-16s) | eBioscience | Cat#15-5773-82; RRID: AB_468806 |
| APC anti-mouse IFNγ (Clone XMG1.2) | Biolegend | Cat#505809; RRID: AB_315403 |

| REAGENT or RESOURCE | SOURCE | IDENTIFIER |
|---|---|---|
| FITC anti-mouse IL-10 (Clone JES5-16ES) | Biolegend | Cat#505006; RRID: AB_315360 |
| PE anti-mouse IL-2 (Clone JES6-5H4) | Biolegend | Cat#503808; RRID: AB_315302 |
| PEcy7 anti-mouse TNFα (Clone MP6-XT22) | Biolegend | Cat#506324; RRID: AB_2256076 |
| FITC anti-mouse CD36 (Clone MF3) | ThermoFisher | Cat# MA5-16832; RRID: AB_2538311 |
| APC anti-mouse CD98 (Clone RL388) | Biolegend | Cat# 128212; RRID: AB_2750545 |
| InVivoMAb anti-mouse CTLA4 (Clone UC10-4F10-11) | BioXcell | Cat# BE0032; RRID: AB_1107598) |
| InVivoMab Armenian hamster IgG (Clone Polyclonal) | BioXcell | Cat# 0091; RRID AB_2687680) |
| InVivoMab anti-mouse CD25 (Clone PC-61.5.3) | BioXcell | Cat# BE0012, RRID:AB_1107619 |
| InVivoMab ratIgGI isotype control (Clone HRPN) | BioXcell | Cat# BE0088, RRID:AB_1107775 |
| InVivoMAb anti-mouse PDL1 (clone 10F.9G2) | BioXcell | Cat#BE0101; RRID:AB_10949073 |
| InVivoMAb rat IgG2b isotype control (clone LTF-2) | BioXcell | Cat#BE0090; RRID:AB_1107780 |
| InVivoMab anti-mouse CD28 (Clone PV-1) | BioXcell | Cat# BE0015-5, RRID:AB_1107628 |
| InVivoMab anti-mouse CD3 ε (Clone 145-2C11) | BioXcell | Cat# BE0001-1, RRID:AB_1107634 |
| Bacterial and virus strains | | |
| LCMV Clone13 | Brooks Lab | |
| LCMV Armstrong | Brooks Lab | |
| Chemicals, peptides, and recombinant proteins | | |
| Cell-ID Cisplatin | Fluidigm | Cat#201064 |
| Cell-ID Intercalator-Irdium—125 mM | Fluidigm | Cat#201192A |
| Cell-ID Intercalator-Rh - 500 μM | Fluidigm | Cat#201103A |
| Zombie Aqua Fixable Viability Kit | Biolegend | Cat#423102 |
| Mouse IL-2 Recombinant Protein | GIBCO | Cat#PMC0025 |
| Mouse GM-CSF | Biolegend | Cat#576304 |
| Mouse IL-4 | Biolegend | Cat#574304 |
| Mouse IL-7 | Biolegend | Cat#577804 |
| Brefeldin A | Sigma | Cat#B7651-5MG |
| DNase I | Sigma | Cat#DN25-1G |
| Cisplatin | BioVision | Cat#1550 |
| Collagenase I | ThermoFisher | Cat#17100017 |
| Fixation Buffer | Biolegend | Cat#420801 |
| Intracellular Staining Permeabilization Wash Buffer (10X) | Biolegend | Cat#421002 |
| Foxp3/Transcription Factor Staining Buffer Set | eBioscience | Cat#00-5523-00 |
| EasySep Mouse $CD4^+$ T cell Isolation Kit | STEMCELL | Cat#19852 |
| 20-Plex Pd Barcoding Kit | Fluidigm | Cat#201060 |
| Mouse CD4 (TIL) Microbeads | Miltenyi Biotec | Cat#130-117-043 |
| Fc block | ThermoFisher | Cat#16-9161-73 |
| MHC class II-restricted LCMV peptide $GP_{61-80}$ | Brooks Lab | |
| P3 Primary Cell 4D-Nucleofector X Kit S | Lonza | Cat# V4XP-3032 |
| TrueCut Cas9 Protein v2 | Thermo Fisher | Cat# A36499 |

| REAGENT or RESOURCE | SOURCE | IDENTIFIER |
|---|---|---|
| TrueGuide™ sgRNA Negative Control, non-targeting 1 | Thermo Fisher | Cat# A35526t |
| 4D-Nucleofector X unit | Lonza | Cat# AAF-1003X |
| In-Fusion HD Cloning Plus kits | TaKaRa | Cat# 638917 |
| lipofectamine 3000 | Thermo Fisher | Cat# L3000001 |
| Diphtheria Toxin | sigma | Cat#D0564-1MG |
| Deposited data | | |
| scRNAseq of mouse CD4 T cells | This manuscript | GEO: GSE211738 |
| Experimental models: Cell lines | | |
| MMTV-PyMT cell line | Dr. Christopher Page (University Health Network) | |
| PyMG tumor cells | Generated by our lab | |
| B16-F10 tumor cells | Dr. Tracy McGaha (University Health Network) | |
| MC38 tumor cells | Dr. Daniel de Carvalho (University Health Network) | |
| MC38-GP cells | Generated by our lab | |
| Oligonucleotides | | |
| TGGCTTGTCTTGGACTCCGG (sgDNA sequence against mouse CTLA4) | TrueGuide™ Synthetic sgRNA (Thermo Fisher Scientific) | |
| GGGACTGTACCTCTGCAAGG (sgDNA sequence against mouse CTLA4) | TrueGuide™ Synthetic sgRNA (Thermo Fisher Scientific) | |
| GACCCAACCTTCAGTGGTGT (sgDNA sequence against mouse CTLA4) | TrueGuide™ Synthetic sgRNA (Thermo Fisher Scientific) | |
| Recombinant DNA | | |
| MSCV-IRES-Thy1.1 DEST vector | Addgene | plasmid# 17442 |
| pCL-ECO vector | Addgene | plasmid# 12371 |
| pSBbi-Pur vector | Addgene | plasmid # 60523 |
| pCMV(CAT)T7-SB100 | Addgene | plasmid # 34879 |

| REAGENT or RESOURCE | SOURCE | IDENTIFIER |
|---|---|---|
| Experimental models: Organisms/strains | | |
| Mouse: C57BL/6J mice | Jackson laboratory | Cat#000664 |
| LCMV-GP33-specific CD8 TCR transgenic (P14) mice | Bred in our facility | |
| LCMV-GP61-specific CD4 TCR transgenic (SMARTA) mice | Bred in our facility | |
| OT_II TCR transgenic mice | Jackson | Stock No: 004194 |
| CD4KO mice | Jackson | Stock No: 002663 |
| FoxP3-DTR mice | Jackson | Stock No: 016958 |
| $\beta_2$m−/− mice | Jackson | Stock No:002087 |
| CTLA4 flox/flox | Ohashi Lab at Princess Margaret Cancer Center | |
| FoxP3$^{eGFP—Cre-ERT2}$ | Jackson | Stock No: 016961 |
| Software and algorithms | | |
| Flow Jo version 9 and 10 | BD FLOWJO | https://www.flowjo.com |
| BD FACSsuite v1.4.0.7047 | BD Biosciences | https://www.bdbiosciences.com |
| Cytobank | Cytobank, Inc | https://www.cytobank.org |
| Graphpad Prism v8 and v9 | GraphPad Software, Inc | https://www.graphpad.com |
| R | R Core Team | https://www.r-project.org |
| UMAP | (McInnes et al., 2018)[65] | RRID:SCR_018217 |
| PhenoGraph | (Levine et al., 2015)[66] | RRID:SCR_016919 |
| diffcyt R | (Weber et al., 2019)[19] | https://bioconductor.org/packages/release/bioc/html/diffcyt.html |
| Ingenuity Pathway Analysis software | Qiagen | |
| SeqGeq software | BD Biosciences | |
| Seurat (v 4.0.4) | (Hao et al., 2001)[67] | https://doi.org/10.1016/j.cell.2021.04.048 |
| GSEA (v.4.2.2) | Broad Institute | |